Synergistic Material-Topography Combinations to Achieve Immunomodulatory Osteoinductive Biomaterials

Laurence Burroughs,[1] Mahetab H. Amer,[1] Matthew Vassey,[1] Britta Koch,[1] Grazziela P Figueredo,[1] Blessing Mukonoweshuro,[1] Paulius Mikulskis,[1] Aliaksei Vasilevich,[2] Steven Vermeulen,[3] Ian L. Dryden,[1] David A. Winkler,[4] Amir M. Ghaemmaghami,[1] Felicity R. A. J. Rose,[1] Jan de Boer§[2] and Morgan R. Alexander§*[1]

§ Joint Senior Authors

* Corresponding Author: Morgan Alexander

Email: morgan.alexander@nottingham.ac.uk

Affiliations

1) University of Nottingham, Nottingham, NG7 2RD, United Kingdom. 2) Eindhoven University of Technology, Eindhoven, 5600 MB, Netherlands. 3) MERLN Institute for Technology, Maastricht, 6229 ER, Netherlands. 4) Medicinal Chemistry, Monash Institute of Pharmaceutical Sciences, Parkville 3052, Australia; La Trobe Institute for Molecular Science, La Trobe University, Bundoora 3042, Australia; CSIRO Data61, Clayton 3168, Australia.

Abstract

Human mesenchymal stem cells (hMSCs) are widely represented in regenerative medicine clinical strategies due to their compatibility with autologous implantation. Effective bone regeneration involves crosstalk between macrophages and hMSCs, with macrophages playing a key role in the recruitment and differentiation of hMSCs. However, engineered biomaterials able to simultaneously direct hMSC fate and modulate macrophage phenotype have not yet been identified. A novel combinatorial chemistry-topography screening platform, the ChemoTopoChip, is used here to identify materials suitable for bone regeneration by screening with human immortalized mesenchymal stem cells (hiMSCs) and human macrophages. The osteoinduction achieved in hiMSCs cultured on the “hit” materials in basal media is comparable to that seen when cells are cultured in osteogenic media, illustrating that these materials offer a materials-induced alternative to osteo-inductive supplements in bone-regeneration. Some of these same chemistry-micro topography combinations also exhibit immunomodulatory stimuli, polarizing macrophages towards a pro-healing phenotype. Maximum control of cell response is achieved when both chemistry and topography are recruited to instruct the required cell phenotype, combining synergistically. The large combinatorial library allows us for the first time to probe the relative cell-instructive roles of microtopography and material chemistry which we find to provide similar ranges of cell modulation for both cues. Machine learning is used to generate structure-activity relationships that identify key chemical and topographical features enhancing the response of both cell types, providing a basis for a better understanding of cell response to micro topographically patterned polymers.

Keywords

biomaterials, mesenchymal stem cells, macrophages, regenerative medicine.

Introduction

Bone repair is a complex and highly organized process involving interactions between multiple cell types, molecular signals, and interactions with the extracellular environment.[1] Currently, autologous bone grafts remain the gold standard in bone regeneration because of their osteogenicity, osteoinductivity, osteoconduction and osteointegration characteristics.[2, 3] Synthetic bone substitutes, such as calcium phosphate (CaP) ceramics, have proven safe and biocompatible but often lack the osteogenicity needed to support bone healing.[4] There is great interest in the use of hMSCs in combination with synthetic biomaterials to provide a potential way of overcoming these challenges in autologous bone grafting.[5, 6]

The inherent multipotency of hMSCs has allowed *in vitro* culture models to be used, in combination with synthetic biomaterials, to differentiate cells into osteoblasts without osteogenic supplements.[7] MSCs have also been shown to form bone *in vivo* driven by nano topography,[5] protein adsorption to surface chemistry[6] and phosphorus delivery to the cells.[8, 9] Furthermore, there is growing evidence demonstrating a reciprocal functional role of macrophage polarization in hMSC osteoblast differentiation, with pro-healing M2 macrophages having previously been reported to enhance hMSC osteoblastic differentiation.[10] The crosstalk between macrophages and MSCs is considered to play a key role in normal bone repair.[11, 12, 13]

Combinatorial screening has been used by the materials community for over 20 years as a tool for identification of biomaterials when the underlying theory required for rational design is undeveloped.[14] Microarrays of polymer spots have successfully identified new materials by determining cell response against large and diverse polymer libraries to identify novel materials supporting pluripotent human embryonic stem cell expansion,[15, 16] and differentiation into cardiomyocytes[17] and hepatocytes.[18] Polymers capable of inducing macrophage polarization[19] or resisting bacterial attachment[20] have also been identified using a similar approach, with devices coated in bacterial resistant polymers recently progressing to clinical trials.[21]

Topographical patterning of surfaces has been shown to direct cell attachment at the microscopic scale.[22] At the nanoscale, phenotypic control has been demonstrated and rationalized in terms of adsorbed protein and effects on cell contractility of focal adhesion formation.[5, 6, 23] Simple geometric shapes such as grooves/ridges, pillars and pits have been investigated;[24, 25] to screen complex microtopographies derived combinatorially, a high-throughput microtopography screening platform, the TopoChip, was developed.[26] This used mathematical algorithms capable of designing millions of possible topographical features from circle, triangle and rectangle primitives (sized 3-23 μm laterally and 10 μm vertically). A subset of these was arranged periodically to form 290 × 290 μm Topo units, which are analogous to the polymer spots in combinatorial chemistry microarrays. A total of 2,176 Topo units were fabricated on each 2 × 2 cm TopoChip using UV photolithography to form a master from which polymers could be embossed with the topographies for cell screening. This allowed a much wider selection of topographies to be screened than previously, freed the process from the constraints of simple geometric form, and used machine-learning to predict new structures likely to elicit desirable cell responses.[26, 27, 28, 29]

The ability to tune or modulate the foreign-body response to a biomaterial is an ongoing challenge in the field of regenerative medicine.[30, 31, 32] This is further complicated when designing materials for tasks such as induction of osteogenic differentiation of hMSCs at the site of implantation. Surface chemistry[15, 16, 33] and surface topography[27, 34, 35, 36] have both been shown to enhance the differentiation and proliferation of stem cells yet, to our knowledge, biomaterials have not been reported capable of simultaneously directing differentiation of hMSCs and polarizing macrophages towards an M2 state. In order to allow the role of both material

chemistry and topography to be surveyed in the field of material-driven bone-regeneration a combinatorial high-throughput screening tool, the *ChemoTopoChip,* was developed in this work.

Materials and Methods

Methacrylate Functionalization of Glass Slides

Glass slides (26 mm × 50 mm × 0.40 mm) are activated using O_2 plasma (p_i = 0.3 mbar, 100 W, 1 min) and immediately transferred into dry (4 Å MS) toluene (50 mL) under argon. 3-(Trimethoxysilyl) propyl methacrylate (1 mL) is added, and the reaction mixture heated to 50°C for 24 h. The slides are then cooled to room temperature and washed by sonication with 3 × 10 mL fresh toluene. The slides are then dried under vacuum in a silicone-free vacuum oven (50°C) for 24 h.

Molding of TMPMP-co-TEGDA Substrate

TEGDA (337 µL) and TMPMP (163 µL) are added together under argon with DMPA (16.9 mg). The mixture is then sonicated for 15 min to ensure mixing. Each ChemoTopoChip mold on the silicon wafer is framed on 3 sides with Scotch tape (3M) spacers, and a methacrylate silanized glass slide placed on top of each ChemoTopoChip to be molded; standard glass microscope slides (25 mm × 75 mm × 1.0 mm) are placed on top as weights to hold the silanized slides in place. The TMPMP/ TEGDA reaction mixture is transferred into an argon glove box (< 2000 ppm O_2) along with the silicon mold, and the monomer solution (60 µL) pipetted between the silicon wafer and silanized slides. The rate of pipetting was manually maintained at a similar rate to that of the capillary forces acting upon the solution. When all ChemoTopoChip positions have been pipetted (~10 min per ChemoTopoChip) they are irradiated with UV light (368 nm, 2 × 15 W bulbs, 10 cm from source) for 10 min. Once complete, the entire molding setup is removed from the glove box and the glass microscope slide weights removed. The silicon wafer is then placed on to a pre-heated (70°C) hot plate; after 10 min, the molded ChemoTopoChips are carefully removed using a scalpel (CAUTION: excessive force and speed will break the thin glass substrate). Once removed, the molded ChemoTopoChips are cleaned by sonication in acetone (10 mL, 10 min) then isopropyl alcohol (10 mL, 10 min). Finally, the ChemoTopoChips are dried under vacuum (0.3 mbar) for 24 hours before functionalization.

Functionalization of Molded ChemoTopoChip Samples

Monomer solutions are made up as follows: 75% v/v in *N*,*N*-dimethylformamide (DMF) for oils; 50% w/v in DMF for solids. Next, 0.05% w/v photoinitiator DMPA is added to these solutions before degassing by sonication (10 min). The molded ChemoTopoChip samples are then transferred into an argon glove box (< 2000 ppm O_2) along with these monomer solutions. A total of 3 µL of monomer solution is then applied to each respective ChemoTopo unit, taking care to evenly cover the entire area required for functionalization. The ChemoTopoChips are then irradiated with UV light (368 nm, 2 × 15 W bulbs, 10 cm from source) for 15 min during which reaction with the surface thiols and polymerization of the monomer occurs, before being removed from the argon glove box and sonicated in isopropanol for 10 min. Due to the lower bond dissociation energy of the acrylate π-bond[37] compared with that of the thiol σ-bond,[38] it is expected that these monomers will polymerize to the thiol moieties on the base TMPMP-co-TEGDA substrate after photoinitiation commences. The samples are then placed under vacuum (0.3 mbar) for 7 days before use.

Time-of-Flight Secondary-Ion Mass Spectrometry (ToF-SIMS) Analysis

ToF-SIMS analysis was carried out using a ToF-SIMS IV (IONTOF GmbH) instrument operated using a 25 kV Bi_3^+ primary ion source exhibiting a pulsed target current of ~1 pA. Samples were scanned at a pixel density of 100 pixels per mm, with 8 shots per pixel over a given area. An ion dose of 2.45 × 10^{11} ions per cm^2 was applied to each sample area ensuring static conditions were

maintained throughout. Both positive and negative secondary ion spectra were collected. Owing to the non-conductive nature of the samples, a low energy (20 eV) electron flood gun was applied to provide charge compensation.

Atomic Force Microscopy (AFM) Analysis
AFM measurements were conducted using a Bruker Dimension FastScan Bio Icon AFM in Peak Force™ (Tapping) mode. Scan areas were 500 × 500 nm and 4 regions of interest (ROIs) were taken. Bruker RTESPA-150 probes were used for all analyses, with all results calibrated to a Bruker polystyrene (2.7 GPa) standard.

X-Ray Photoelectron Spectroscopy (XPS) Analysis
XPS characterization was carried out using a Kratos AXIS ULTRA. Data was processed using CasaXPS version 2.3.20 rev1.2G. Estimation of the functionalized surface layer thickness of the iBOMAm region was carried out using the method described by Ray and Shard as follows:[39]

$$d_{N(1s)} = -L_{N(1s)}\, cos\theta\, ln\left(1 - \frac{[N]-[N]_0}{[N]_\infty-[N]_0}\right) \quad \text{(Eq 1)}$$

$$L = 0.00837\, E^{0.842} \quad \text{(Eq 2)}$$

Where $L_{N(1s)}$ is the average polymer electron attenuation length (3.01 nm) calculated from the electron kinetic energy of the N1s electrons E (1085.5 eV), θ is the electron take-off angle (0°), $[N]$ is the nitrogen atomic fraction in the measured sample layer (1.08%), $[N]_0$ is the nitrogen atomic fraction in the pure substrate layer (0%), $[N]_\infty$ is the nitrogen atomic fraction in the pure sample layer (9.10%).

Mesenchymal Stem Cell Culture
Human immortalized mesenchymal stem cells (hiMSCs) were generated in-house by lentiviral transfection of E6/E7 and hTERT genes as previously described.[40, 41] Cells were cultured in Dulbecco's modified Eagle's medium supplemented with 10% (v/v) foetal bovine serum, 1% (v/v) penicillin-streptomycin and 1% L-glutamine (Basal media). Positive controls were cultured in Human Mesenchymal Stem Cell (hMSC) Osteogenic Differentiation Medium (PT-3002; Lonza), which is supplemented with dexamethasone, L-glutamine, ascorbate, penicillin/streptomycin and β-glycerophosphate. All cells were maintained in a humidified incubator at 37°C and 5% CO_2 in air. Cells were re-suspended in the appropriate volume of media and seeded on 3 replicate ChemoTopoChips at 1 × 10^5 hiMSCs/chip (3 independent experiments using cells from 3 different passage numbers).

hiMSC Immunofluorescence Staining
For alkaline phosphatase (ALP) staining, cells were cultured on the ChemoTopoChips for five days in culture medium (at 37°C, 5% CO_2 in air), then fixed using 70% (v/v) ethanol, permeabilized with 0.1% (v/v) Triton X-100 and incubated with a blocking solution of 3% (v/v) goat serum in 1% (v/v) BSA/PBS. Staining was carried out using human ALP antibody (Dilution 1:50; sc137213, Santa Cruz Biotech) and counterstained for α-tubulin (2 µg/mL; PA120988, Invitrogen) for 3 hours at room temperature. After washing, slides were incubated with the appropriate secondary antibodies in the green and red channels at room temperature (1:100 dilution). Nuclei were stained with NucBlue Fixed Cell ReadyProbes™ (Invitrogen).

Monocyte Isolation and Culture
Buffy coats were obtained from the National Blood Service after obtaining written informed consent and approval from the ethics committee. Monocytes were isolated from peripheral blood mononuclear cells (PBMCs). A MACS magnetic cell separation system (CD14 MicroBeads positive selection with LS columns, Miltenyi Biotec) was used for the isolation as previously described.[19, 42] Isolated monocytes (>95% purity) were suspended in RPMI-1640 medium containing 10% foetal bovine serum (FBS), 100 µg/ml streptomycin, 2mM L-glutamine and 100 U/ml penicillin (Sigma-Aldrich). For assessment of cell attachment and phenotype characterization, cells were re-suspended in the appropriate volume of media and

seeded on the ChemoTopoChips at 2 × 10^6 monocytes/chip and incubated at 37˚C, 5% CO_2 in a humidified incubator for 9 days.

Macrophage Immunofluorescent Staining
On day 9 all adherent cells cultured on ChemoTopoChips were fixed in 4% paraformaldehyde (BioRad) in PBS, then blocked with 3% BSA (Sigma-Aldrich) and 1% Glycine (Fisher Scientific) in PBS. Subsequently, another blocking step was carried out using 5% goat serum (Sigma) in PBS. Adherent cells were stained with 2 µg/mL anti-human TNFα (IgG1) mAb (Abcam), and with 1 µg/ml anti-human IL-10 (IgG1) mAb (Abcam) followed by 1 h incubation at room temperature. After washing, cells were stained with 8 µg/ml Rhodamine-x goat anti-mouse IgG (H+L) secondary Ab (Invitrogen), and 8 µg/ml Alexa flour-647 goat anti-rabbit IgG (H+L) secondary antibody (Invitrogen) for another hour at room temperature. All samples were counterstained with 250 ng/ml DAPI (4',6-Diamidino-2-Phenylindole) (Invitrogen) at room temperature.

ChemoTopoChip Imaging
Imaging of all fixed and stained ChemoTopoChip samples was carried out using a widefield deconvolution-TIRF3 system (Zeiss, custom setup). Imaging was carried out in wide field mode using a 20×/0.5 NA air objective in the bright field and fluorescence channels with the excitation at 358 nm, 488nm and 561 nm. The software used to capture was Zeiss Zen Blue, by using the "Sample Carrier Designer" wizard/module to manually create and calibrate the position list which was used to scan all the positions in the chip setup.

CellProfiler Analysis
A custom CellProfiler[43] pipeline was created to correct for uneven background illumination in each image, then each image cropped to within the Topo unit 30 µm wall. Nuclei were detected using an adaptive per-object algorithm in the blue channel images, followed by propagation from these primary detected objects to detect cell cytoskeleton and ALP staining (hiMSCs) or TNFα and IL-10 (human macrophages) in the green and red channel images. Intensity of detected objects was measured and exported, and images containing overlaid outlines of detected objects also saved to ensure correct operation of the pipeline.

Statistical Analysis
Statistical analysis and graphical plots were carried out in R version 3.6.1 using RStudio version 1.2.1335 as integrated development environment (IDE). For an exploratory method, combinations having p-value < 0.05 were highlighted from a two independent sample equal variance t-test. Note that the sample sizes are small here and this does not account for multiple tests. The values were normalized to the base polymer region on each slide. Heatmaps were plotted using the heatmap.2 function from the gplots package version 3.1.0.2 in combination with the RColorBrewer package version 1.1-2. Clustering and dendrograms for heatmaps were produced using the complete linkage method[44] with Euclidean distance measure. Ranked scatter plots and box plots were carried out using base functions in R and the ggplot2 package version 3.2.1.

Synergy Ratio Determination
Assessment of the interactions between binary factors (chemistry and topography) is readily performed using a synergy ratio (*SR*). Taking the response of factor x_1 alone (y_1), the response of factor x_2 alone (y_2) and the response of the factors combined x_{12} (y_{12}), *SR* can be calculated as shown in Equation Eq 3:

$$SR = \frac{y_{12}}{y_1 + y_2} \quad \text{(Eq 3)}$$

For a synergistic combination, *SR* > 1 as the ratio is then greater than the sum of the theoretical maximums of the individual response factor comparators; for a counteractive combination, SR < 0.5 as the ratio is then less than the theoretical maximum of one individual response factor alone (i.e. 0 contribution from the second individual response factor). In analysis of the ChemoTopoChip data, unfunctionalized TMPMP-co-TEGDA molded topographies and flat area

chemistries were used as the individual factors x_1 and x_2 to compare with the hit topography-material combinations x_{12}.

Random Forest Machine Learning

The raw dataset consisted of three technical repeats for each surface variable (topography, chemistry) within a chip, which were further replicated across multiple batches (biological repeats). Data set from repeats in a chip have been normalized against their correspondent flat values. Subsequently, replicate average values were calculated. The average between batches was then determined as the dependent variable for the predictive models. Macrophage polarization and ALP intensity predictive models were generated.

The various topographies were encoded using descriptors generated by CellProfiler[43] that relate directly to particular primitives in the topographical units. For chemistries, 1-hot descriptors (binary variables indicating the presence or absence of a chemistry in any given combination) were used.

The SHapley Additive exPlanation (SHAP) method was used for feature selection to eliminate uninformative and less informative descriptors and less relevant chemistries. SHAP was implemented using the SHAP package in Python 3.7. Regression models were generated using the random forest approach with the scikit-learn package in Python 3.7. The default parameters from version 0.22 were adopted for the random forest models. That is, 100 estimators were considered using gini as the function to measure the quality of the data instances split. And no limit for the maximum depth of the trees was defined. 70% of the data instances were employed for model training and 30% for testing. The performance of the predictive models and the topographical descriptors that contributed most strongly to the attachment and polarization are shown in **Figure 3**. The figure presents the results of the regression models as well as the features selected. The features are ordered from top to bottom based on their average impact on the model output magnitude

Results and Discussion

The ChemoTopoChip design is presented in Figure 1 (a-c). This platform contains 1008 microtopography and materials chemistry combinations to simultaneously probe their combined effects on cellular response. This is effectively a combination of the polymer microarray approach and the TopoChip platforms to facilitate identification of synergistic chemistry-topography combinations, and elucidation of structure-function relationships between cells and material cues.

The design comprised 36 Topo units of size 500 × 500 μm, including one flat control (Figure 1b) arranged in 3 × 3 mm sized ChemoTopo units. These are repeated 28 times, each with a different chemical functionalization. The microtopographies are 10 μm high and were chosen from previous TopoChip screens to maximize the morphological differences of MSCs (see Figure S1 for high-resolution images).[36] The chemistries were chosen from libraries of (meth)acrylate and (meth)acylamide monomers to provide maximum chemical diversity (see Figure S2 for structures). The monomers are used to functionalize the surface of topographically molded chips, which minimizes differences in material compliance between the different chemistries. The modulus measured by AFM was found not to vary greatly as anticipated for surface modification of the underlying polymer (Table S1).

A silicon mold was fabricated from the ChemoTopoChip design using photolithography and etching to produce the negative master of the topographies. The desired features were produced from this master by injecting a 1:2 mixture of trimethylolpropane tri(3-mercaptopropionate): tetra(ethylene glycol) diacrylate (1:2 TMPMP:TEGDA) monomers containing the photoinitiator 2,2-dimethoxy-2-phenylacetophenone (DMPA) between a methacrylate-functionalized glass slide

and the silicon master. UV curing and solvent washing then provided the molded ChemoTopoChip substrate, chosen because similar photopolymerized thiol-ene systems have been reported as tough shape memory, flexible materials offering low shrinkage stress that are sufficiently transparent to allow transmission optical imaging.[45] Functionalization of the ChemoTopo units was carried out by deposition of 50% w/v or 75% v/v monomer solutions in *N*,*N*-dimethylformamide (DMF) containing 0.05% w/v DMPA onto each ChemoTopo unit prior to UV curing and washing. Imaging surface analysis (ToF-SIMS) was used to determine to localization of the chemistries, which were found to be confined to the desired areas in Figure S3. Elemental and functional composition was determined by XPS and found to be consistent with the expected surface chemical modification for an amide where the nitrogen signal increases, Figure S4. Estimation of the surface layer thickness using the nitrogen composition of the monomer for an acrylamide provided a value of approximately 0.4 nm.[39]

hiMSC differentiation

To identify materials that can direct hiMSC differentiation towards an osteoblastic lineage and that induce human macrophages polarization towards a pro-healing M2 phenotype, we first investigated the osteoinductive potential of the materials. hiMSCs were seeded on 3 replicate chips in 3 independent experiments and cultured in basal culture media. This culture media was not supplemented with any exogenous osteo-inductive factors. After 5 days, samples were fixed and stained for both α-tubulin (cytoskeletal marker) and alkaline phosphatase (ALP, an early osteogenic marker), and analyzed using an automated high-throughput fluorescence microscope. ALP expression is a widely used early osteogenesis marker as it is known to be involved in bone formation, plays an essential role in matrix mineralization and is induced by a range of osteogenic molecules.[46] Images were processed using CellProfiler software[43] to quantify cell number and ALP staining intensity on each individual topography-material combination. The ALP staining intensity and attached cell number were both normalized to that of the flat TMPMP-co-TEGDA Topo unit within each ChemoTopoChip sample.

A diverse range of hiMSC morphologies and attached cell numbers were seen across the ChemoTopoChip. The stem cells displayed an elongated shape and on some ChemoTopo units with alignment to the topographies, e.g. as seen in Figure 1e**,** in contrast to more uniform cell spreading and random alignment on others and on the flat chemistry as seen in Figure 1d. The stem cell response to iBOMAm and the base TMPMP-co-TEGDA chemistries are presented in Figures S5 and S6 to illustrate the variation in cell morphology and alignment**.** Previous TopoChip screens using hMSCs revealed a similar range of cell morphological responses, where more elongated cells were linked to ALP upregulation.[27, 36]

To ascertain the magnitude of the ALP upregulation we compared the fluorescence intensity per cell of the hiMSC cells differentiated in osteo-inductive media with the response of cells cultured in basal media on the chip (supplements detailed in Materials and Methods). No difference in ALP upregulation was observed between the top 50 ChemoTopoChip ALP hits and the positive control sample cultured in osteogenic media ($p < 0.001$, see Figure 2). These materials therefore induce a similar osteogenic state of the cells, as measured by ALP upregulation, to that of osteo-inductive supplements commonly used to differentiate hMSCs to osteoblasts. In the absence of stimulatory materials chemistry-topography combinations, the ALP intensity was significantly lower as seen for the lowest 50 combinations.

To interrogate the range and magnitude of the cell effects from this large range of chemo-topo combinations, we found it is useful to plot all the results as both heatmaps (Figure 3a) and as rank ordered plots to illustrate the range of cell response for all ChemoTopo units (Figure 3c). To focus the data interrogation, we indicate the combinations which were determined to have p-value < 0.05 from a two independent sample equal variance t-test, although we note that the sample sizes are relatively small here and this does not account for the *multiple comparisons problem* for the large number of different substrates compared. Analysis of the mean integrated ALP

expression per cell for each topography-material combination showed that 113 exhibited significant upregulation of this osteogenic marker ($p < 0.05$) compared to the flat base Topo unit (see Table S2 for full list), with all of these displaying a higher ALP intensity than the flat base material region used as a control comparator. Visual inspection of the heatmaps and ranked scatter plots reveals trends across various chemistries, e.g. monomers 12 (mono-2-(methacryloyloxy)ethyl succinate, mMAOES) and 20 (*N*-tert-octylacrylamide, tOcAm), suggesting that a group of chemistries induce upregulation of ALP intensity relative to the mean; equivalent topographical trends were less evident indicating that topographical stimuli did not dominate across the range of chemistries used (see Figure 3a and Figure 3c). A total of 103 combinations were found to have higher normalized cell number than the flat base region used as the control ($p < 0.05$, total area taken into account), but none lower (Table S2 for full list). All combinations containing topographies that showed greater cell numbers than those of chemistries on flat surfaces (Topo 1), suggesting that topography was also a driver for hiMSC attachment (see Figure S7 and Figure S8a).

Macrophage Polarization

The immunomodulation effect of material-topography combinations was screened by seeding primary human monocytes onto ChemoTopoChips for 6 days followed by cell counting and immunohistochemical fluorescent readouts to estimate differentiation into macrophages and polarization to the M1 or M2 phenotype. Monocytes were isolated from peripheral blood of two independent donors, with 3 replicates carried out for each. To determine the polarization status of the cells, samples were fixed and stained for intracellular expression of the pro- and anti-inflammatory cytokines tumor necrosis factor α (TNFα, M1 polarization indicator) and interleukin-10 (IL-10, M2 polarization indicator) respectively, and analyzed using high-throughput fluorescence microscopy. Images were processed using CellProfiler software[43] with an image analysis pipeline designed to quantify cell attachment using DAPI nuclear staining and quantification of the mean fluorescence intensity (MFI) across each Topo unit for the IL-10 and TNFα channels. The IL-10 and TNFα MFI and cell number were normalized to the values from the flat base TMPMP-co-TEGDA Topo unit. The ratio of M2/M1 cells was taken to be the ratio of the IL-10/TNFα MFIs.

Plotting the normalized macrophage cell number and M2/M1 ratio as a scatter plot rank ordered by topography (Figure 3d) and as heatmaps (Figure 3b) indicated that chemistry may have a greater influence over human macrophage polarization than topography. This is in large part due to the significant influence of the M2/M1 ratio provided by material chemistries: 2-(4-benzoyl-3-hydroxyphenoxy)ethyl acrylate (BzHPEA), *N*,*N*'-dimethylacrylamide (DMAm) and heptadecafluorodecyl acrylate (HDFDA). These chemistries showed high M2 polarization across a majority of topographies in the ranked scatter plots (Figure 3d). Horizontal trends across these chemistries could be seen in the heatmap (Figure 3b), with vertical trends across topographies less apparent. Similar ranges of responses were observed for all topography-material combinations, including those containing flat areas. As was seen with hiMSC attachment, the range of normalized cell number for combinations containing topographies was greater than those for flat areas (see Figure S9 and Figure S8c); topography is therefore also found to be important for macrophage attachment. Visual inspection identified some topography-material combinations that were hits for both stem cell differentiation and polarizing macrophages to anti-inflammatory phenotype, with BzHPEA (chemistry 7) in combination with topography 22 appearing strongest for both ALP upregulation in hiMSCs and M2 polarization in macrophages (Figure 3a-d).

To assess the influence of topography and chemistry, flat chemistries and unfunctionalized TMPMP-co-TEGDA molded topographies were used as comparators. Hit topography-material combinations were compared to these controls to assess their synergy ratios (*SR*). For the hiMSC data set, 15 of the 103 hit combinations that showed greater cell numbers than the flat TPMP-co-TEGDA control were determined to be synergistic (Figure 4a); additionally, 2 of the 113

hit combinations directing osteogenic differentiation were determined to be synergistic (Figure 4b). For the hiMSC cell number, 2 combinations appeared to be antagonistic (Figure 4a). For the human macrophage cell number, 2 topography-material combinations exhibited a synergistic effect (Figure 4c). Of the top 22 human macrophage polarization combinations, 4 were determined to be synergistic (Figure 4d). A total of 3 combinations were found to promote upregulation of ALP in hiMSCs *and* polarize human macrophages towards an M2 phenotype (Figure 4b, d-f). The chemistries from these combinations (Figure 4e), mMAOES and BzHPEA, respectively contain carboxylic and phenolic groups in combination with ethylene glycol units. This may point to the influence of surface charge for both hiMSC ALP upregulation and macrophage polarization. Visual inspection of the synergistic topographies (Figure 4f) did not indicate any obvious correlation between the patterns. The top material, BzHPEA in combination with Topo 22, was found to be synergistic for both datasets (Figure 4b, d).

To investigate the feasibility of extracting rules from ChemoTopoChip screening data to inform future materials development, we used machine learning (ML) methods to generate quantitative structure-activity relationships. A combination of chemistry descriptors, “1-hot” binary variables indicating the presence or absence of a chemistry in any given combination, and topographical shape descriptors generated from CellProfiler[43] were used to model both data sets using the Random Forest algorithm[47] (Figure 5). The 1-hot encoding method generates a vector with length equal to the number of categories in the data set. If a particular category is present, that category’s position is set to 1 and all other positions in the vector are zero. Thus, 1-hot encoding is a process for converting categorical variables into a form that machine learning algorithms can use to generate predictive models.

The macrophage M2/M1 ratio model had a strong correlation between the ML-predicted and observed values (R^2 = 0.73, Figure 5a). The size of the topographical features was identified as being important for macrophage polarization. Features with mean areas < 50 μm^2 and maximum radii of 1-3 μm generated highest M2/M1 ratio (see Figure S10 for polarization vs. descriptor rank order plots). The circularity of the topographical features was a strong contributor to the model, with smaller eccentricities producing the greatest increase in macrophage M2 polarization (Figure S10c). Topographical descriptors had a greater impact on the M2/M1 human macrophage model than on the hiMSC ALP intensity model (i.e. topography plays a larger role in macrophage polarization than in hiMSC osteoinduction). This is consistent with the phagocytic nature of macrophage cells, which engulf bacterial cells and small particles. These analyses illustrate the potential of the ChemoTopoChip and ML for uncovering complex relationships between topography, chemistry, and cell response that offer opportunities for bespoke cell phenotype control using materials design alone.

The hiMSC ALP intensity Random Forest model produced a relatively low correlation between predicted and observed ALP induction (R^2 = 0.46, Figure 5b). Difficulties in modelling stem cell responses in polymeric biomaterials has been noted previously,[15] in that case due to a relatively small number of polymers with diverse chemotypes driving desirable cell responses. There were therefore insufficient examples of each chemical feature for the ML models to generate rules from. Topographical descriptors identified as being important in the hiMSC ALP model included the size of the topographical features (Table S4 contains list of feature descriptions), with features ≤ 3.5 μm radius increasing ALP expression. However, this trend was not as strong as that observed for macrophage polarization (see Figure S11 for ALP upregulation vs. descriptor rank order plots) where cylindrical features of ≤ 3 μm radius increased M2 polarization. Orientation of topographical features also contributed to the model, with those having a small number (< 10%) of features rotated > 25° relative to the x-axis of the Topo unit walls driving an increase in ALP expression.

In polystyrene TopoChip screening of macrophage response, cylindrical pillars with feature size of 5-10 μm radius have also been shown to promote M2 polarization.[29] However, in that work

the entire TopoChip selection of 2,176 topographies[26] was screened on a polystyrene substrate, in contrast with this study where a selection of 35 topographies (chosen from MSC morphological clustering[36]) were screened in combination with 28 different substrate chemistries. The influence of chemistry, and subset of topographies screened, may account for the small differences in findings between these two studies.

In previous modelling studies of biological responses to polymer libraries, *signature* and other fragment-based molecular descriptors and *Dragon* molecular descriptors have been shown to represent surface chemistries well. These descriptors generated robust, predictive models for diverse biological responses.[48] Paradoxically, in the current study, these types of chemical descriptors were unable to generate ML models for the ChemoTopoChip data that were as accurate as the models using simple 1-hot descriptors to encode the identities of the polymer chemistries. We propose that this is due to the great diversity of the 28 chemistries on the ChemoTopoChip, chosen in order to cover chemical space as widely as possible. The key chemical fragments and resultant descriptors are also therefore very sparse. ML models cannot learn features that are not sufficiently represented in the data set, hence the combination of high chemical diversity and low number of samples resulted in inadequate information on which to train the ML models, resulting in lower prediction accuracies.

Conclusions

We have developed the novel ChemoTopoChip platform to screen the potential of both chemistry and topography in producing immunomodulatory materials suitable for bone regenerative applications. Analysis of the hiMSC and human macrophage datasets has identified a range of novel chemistry-topography combinations that surpass the material-instructive cues provided by either alone, with 2-(4-benzoyl-3-hydroxyphenoxy)ethyl acrylate in combination with Topo 22 being synergistic for both cell types. Attachment of both cell types and the hiMSC alkaline phosphatase (ALP) upregulation spanned similar ranges for the large range of chemistries and microtopographies studied, but macrophage polarization was more strongly influenced by chemistry than topography. This large survey of this parameter space allows us to conclude that both chemical and topographical features are important drivers when designing biomaterials for simultaneous control of multiple cell types and act synergistically in some cases. Modelling of the human macrophage polarization data showed that small, cylindrical pillars of < 3 μm radius directed macrophage polarization towards an anti-inflammatory phenotype. The size and orientation of topographical features was also important for hiMSC ALP expression, with features of ≤ 3.5 μm radius and rotation of $> 25°$ relative to the x-axis of the Topo units providing strongest upregulation of ALP. Data generated by the ChemoTopoChip has been shown to be very amenable to machine learning methods, facilitating the development of structure-activity relationships. The methodology illustrated here is equally applicable to other adhesion dependent cells to aid in the design of cell-instructive materials.

Acknowledgments

This research is supported by funding from the Engineering Physical Sciences Research Council (EPSRC) under the Programme Grant Next Generation Biomaterials Discovery EP/N006615/1. AV, SV and JdB are funded by the European Union's Seventh Framework Programme (FP7/2007-2013) under grant agreement no 289720. AV acknowledge the financial contribution of the Province of Limburg. SV acknowledges the financial support of the European Union’s Horizon 2020 Programme (H2020-MSCA- ITN-2015; Grant agreement 676338).

The authors would like to thank Dr Chris Gell (School of Life Sciences Imaging and Microscopy (SLIM) Facility) for assistance with high throughput microscopy.

Author Contributions

This manuscript was written with contributions from all authors. LB manufactured and characterized ChemoTopoChips, carried out image analysis and statistical analysis of results. MHA carried out hiMSC experiments and imaging, MV and BM carried out macrophage experiments and imaging. BK, PM, AS and SV developed the initial ChemoTopoChip platform. GPF and DW performed modelling of data. ILD provided assistance with statistical analysis. AMG, FRAJR, JdB and MRA oversaw project from design to implementation.

Disclosure of potential financial conflicts

Jan de Boer is a founder and shareholder of Materiomics b.v.

Data Availability

Raw cell data files, CellProfiler pipelines and topographical descriptors are available in the **Data Repository**. Experimental procedures are detailed in the **Materials and Methods** section; supplementary figures and processed data tables are available in the **Supplementary Data** section.

References

[1] Harada S., Rodan G. A., Control of osteoblast function and regulation of bone mass. *Nature*, 423 (2003) 349-355.
[2] Greenwald A. S., Boden S. D., Goldberg V. M., Khan Y., Laurencin C. T., Rosier R. N., Bone-graft Substitutes: Facts, Fictions, and Applications. *J. Bone Joint Surg. Am.*, 83 (2001) 98-103.
[3] Moshiri A., Oryan A., Shahrezaee M., An Overview on Bone Tissue Engineering and Regenerative Medicine: Current Challenges, Future Directions and Strategies. *J. Sports Med. Doping Stud.*, 5 (2015) 1000e144.
[4] Samavedi S., Whittington A. R., Goldstein A. R., Calcium Phosphate Ceramics in Bone Tissue Engineering: A Review of Properties and Their Influence on Cell Behavior. *Acta Biomater.*, 9 (2013) 8037-8045.
[5] Dalby M. J., Gadegaard N., Tare R., Andar A., Riehle M. O., Herzyk P., Wilkinson C. D., Oreffo R. O., The control of human mesenchymal cell differentiation using nanoscale symmetry and disorder. *Nat. Mater.*, 6 (2007) 997-1003.
[6] Ngandu Mpoyi E., Cantini M., Reynolds P. M., Gadegaard N., Dalby M. J., Salmerón-Sánchez M., Protein adsorption as a key mediator in the nanotopographical control of cell behavior. *ACS Nano.*, 10 (2016) 6638-6647.
[7] Dawson E., Mapili G., Erickson K., Taqvi S., Roy K., Biomaterials for stem cell differentiation. *Adv. Drug Deliv. Rev.*, 60 (2008) 215-228.
[8] Wang D.A., Williams C.G., Yang F., Cher N., Lee H., Elissee J.H., Bioresponsive phosphoester hydrogels for bone tissue engineering. *Tissue Eng.*, 11 (2005) 201-213.
[9] Nuttelman C.R., Tripodi M.C., Anseth K.S., Synthetic Hydrogel Niches That Promote hMSC Viability. *Matrix Biol.*, 24 (2005) 208-218.

[10] Gong L., Zhao Y., Zhang Y., Ruan Z., The Macrophage Polarization Regulates MSC Osteoblast Differentiation in Vitro. *Ann. Clin. Lab. Sci.*, 46 (2016) 65-71.
[11] Loi F., Córdova L. A., Pajarinen J., Lin T., Yao Z., Goodman S. B., Inflammation, fracture and bone repair. *Bone*, 86 (2016) 119-130.
[12] Sridharan R., Cameron A. R., Kelly D. J., Kearney C. J., O'Brien F. J., Biomaterial based modulation of macrophage polarization: A review and suggested design principles. *Mater. Today*, 18 (2015) 313-325.
[13] Mariani E., Lisignoli G., Borzi R. M., Pulsatelli L., Biomaterials: Foreign Bodies or Tuners for the Immune Response? *Int. J. Mol. Sci.*, 20 (2019) 636.
[14] Kohn J. New approaches to biomaterials design. *Nat. Mater.*, 3 (2004) 745-747.
[15] Celiz A. D., Smith J. G. W., Patel A. K., Hook A. L., Rajamohan D., George V. T., Patel M. J., Epa V. C., Singh T., Langer R., Anderson D. G., Allen N. D., Hay D. C., Winkler D. A., Barrett D. A., Davies M. C., Young L. E., Denning C., Alexander M. R., Discovery of a Novel Polymer for Human Pluripotent Stem Cell Expansion and Multilineage Differentiation. *Adv. Mater.*, 27 (2015) 4006-4012.
[16] Zhang R., Mjoseng H. K., Hoeve M. A., Bauer N. G., Pells S., Besseling R., Velugotla S., Tourniaire G., Kishen R. E. B., Tsenkina Y., Armit C., Duffy C. R. E., Helfen M., Edenhofer F., de Sousa P. A., Bradley M. A thermoresponsive and chemically defined hydrogel for long-term culture of human embryonic stem cells. *Nat. Commun.*, 4 (2013) 1335.
[17] Patel A. K., Celiz A. D., Rajamohan D., Anderson D. G., Langer R., Davies M. C., Alexander M. R., Denning C. A defined synthetic substrate for serum-free culture of human stem cell derived cardiomyocytes with improved functional maturity identified using combinatorial materials discovery. *Biomaterials*, 61 (2015) 257-265.
[18] Hay D. C., Pernaglio S., Diaz-Mochon J. J., Medine C. N., Greenhough S., Hannoun Z., Schrader J., Black J. R., Fletcher J., Dalgetty D., Thompson A. I., Newsome P. N., Forbes S. J., Ross J. A., Bradley M., Iredale J. P. Unbiased screening of polymer libraries to define novel substrates for functional hepatocytes with inducible drug metabolism, *Stem. Cell. Res*., 6 (2011) 92-102.
[19] Rostam H. M., Fisher L. E., Hook A. L., Burroughs L., Luckett J. C., Figueredo G. P., Mbadugha C., Teo A. C. K., Latif A., Kämmerling L., Day M., Lawler K., Barrett D., Elsheikh S., Ilyas M., Winkler D. A., Alexander M. R., Ghaemmaghami A. M., Immune-Instructive Polymers Control Macrophage Phenotype and Modulate the Foreign Body Response In Vivo. *Matter*, 2 (2020) 1564-1581.
[20] Hook A. L., Chang C. Y., Yang J., Luckett J., Cockayne A., Atkinson S., Mei Y., Bayston R., Irvine D. J., Langer R., Anderson D. G., Williams P., Davies M. C., Alexander M. R. Combinatorial discovery of polymers resistant to bacterial attachment. *Nat. Biotechnol*., 30 (2012) 868-875.
[21] Jeffery N., Kalenderski K., Dubern J., Lomiteng A., Dragova M., Frost A., Macrae B., Mundy A., Alexander M., Williams P., Andrich D. A new bacterial resistant polymer catheter coating to reduce catheter associated urinary tract infection (CAUTI): A first-in-man pilot study. *Eur. Urol. Suppl.*, 18 (2019) e377.
[22] Curtis A., Wilkinson C. Topographical control of cells. *Biomaterials*, 18 (1997) 1573-1583.
[23] Amin Y. Y., Runager K., Simoes F., Celiz A., Taresco V., RosR., Enghild J. J., Abildtrup L. A., Kraft D. C., Sutherland D. S., Alexander M. R., Foss M., Ogaki R. Combinatorial Biomolecular Nanopatterning for High-Throughput Screening of Stem-Cell Behavior. *Adv. Mater.*, 28 (2016) 1472-1476.
[24] Roach P., Parker T., Gadegaard N., Alexander M. R. A bio-inspired neural environment to control neurons comprising radial glia, substrate chemistry and topography. *Biomater. Sci.*, 1 (2013) 83-93.
[25] Yang J., Rose F. R. A. J., Gadegaard N., Alexander M. R. A High-Throughput Assay of Cell-Surface Interactions using Topographical and Chemical Gradients. *Adv. Mater.*, 21 (2009) 300-304.

[26] Unadkat, H. V., Hulsman M., Cornelissen K., Papenburg B. J., Truckenmüller R. K., Carpenter A. E., Wessling M., Post G. F., Uetz M., Reinders M.J. T., Stamatialis D., van Blitterswijk C. A., de Boer J. An algorithm-based topographical biomaterials library to instruct cell fate. *Proc. Natl. Acad. Sci. USA*, 108 (2011) 16565-16570.
[27] Hulshof F. F. B., Papenburg B., Vasilevich A., Hulsman M., Zhao Y., Levers M., Fekete N., de Boer M., Yuan H., Shantanu S., Beijer N., Bray M. A., Logan D. J., Reinders M., Carpenter A. E., van Blitterswijk C., Stamatialis D., de Boer J. Mining for osteogenic surface topographies: In silico design to in vivo osseo-integration. *Biomaterials*, 137 (2017) 49-60.
[28] Vasilevich A. S., Mourcin F., Mentink A., Hulshof F., Beijer N., Zhao Y., Levers M., Papenburg B., Singh S., Carpenter A. E., Stamatialis D., van Blitterswijk C., Tarte K., de Boer J. Designed Surface Topographies Control ICAM-1 Expression in Tonsil-Derived Human Stromal Cells. *Front. Bioeng. Biotechnol*., 6 (2018) 87.
[29] Vassey M. J., Figueredo G. P., Scurr D. J., Vasilevich A. S., Vermeulen S., Carlier A., Luckett J., Beijer N. R. M., Williams P., Winkler D. A., de Boer J., Ghaemmaghami A. M., Alexander M. R. Immune Modulation by Design: Using Topography to Control Human Monocyte Attachment and Macrophage Differentiation. *Adv. Sci.*, 7 (2020) 1903392.
[30] Chandorkar Y., K R., Basu B., The Foreign Body Response Demystified. *ACS Biomater. Sci. Eng.*, 5 (2019) 19-44.
[31] Vegas A.J., Veiseh O., Gürtler M., Millman J. R., Pagliuca F. W., Bader A. R., Doloff J. C., Li J., Chen M. Olejnik K., Tam H. H., Jhunjhunwala S., Langan E., Aresta-Dasilva S., Gandham S., McGarrigle J. J., Bochenek M. A., Hollister-Lock J., Oberholzer J., Greiner D. L., Weir G. C., Melton D. A. Langer R., Anderson D. G. Long-term glycemic control using polymer-encapsulated human stem cell–derived beta cells in immune-competent mice. *Nat. Med*., 22 (2016) 306-311.
[32] Doloff J. C., Veiseh O., Vegas A. J., Tam H. H., Farah S., Ma M., Li J., Bader A., Chiu A., Sadraei A., Aresta-Dasilva S., Griffin M., Jhunjhunwala S., Webber M., Siebert S., Tang K., Chen M., Langan E., Dholokia N., Thakrar R., Qi M., Oberholzer J., Greiner D. L., Langer R., Anderson, Daniel G. Colony stimulating factor-1 receptor is a central component of the foreign body response to biomaterial implants in rodents and non-human primates. *Nat. Mater.*, 16 (2017) 671-680.
[33] Celiz A. D., Smith J. G. W., Langer R., Anderson D. G., Winkler D. A., Barrett D. A., Davies M. C., Young L. E., Denning C., Alexander M. R. Materials for stem cell factories of the future. *Nat. Mater.*, 13 (2014) 570-579.
[34] Li D., Zheng Q., Wang Y., Chen H., Combining surface topography with polymer chemistry: exploring new interfacial biological phenomena. *Polym. Chem.*, 5 (2014) 14-24.
[35] Li Q., Zhang B., Kasoju N., Ma J., Yang A., Cui Z., Wang H., Ye H., Differential and Interactive Effects of Substrate Topography and Chemistry on Human Mesenchymal Stem Cell Gene Expression. *Int. J. Mol. Sci.*, 19 (2018) 2344.
[36] Vasilevich A., Vermeulen S., Kamphuis M., Roumans N., Eroume S., Hebels D. G. A. J., Reihs R., Beijer N., Carlier A., Carpenter A. E., Singh S., de Boer J., *in preparation*.
[37] Miller S. I., Dissociation energies of π-bonds in alkenes. *J. Chem. Educ.*, 55 (1978) 778-780.
[38] Darwent B. de B., Bond Dissociation Energies in Simple Molecules. *National Standard Reference Data Series,* National Bureau of Standards 31, Washington, 1970.
[39] Ray S., Shard A. G., Quantitative Analysis of Adsorbed Spectroscopy. *Anal. Chem.*, 83 (2011) 8659-8666.
[40] Balducci L., BlaA., Saldarelli M., Soleti A., Pessina A., Bonomi A., Coccè V., Dossena M., Tosetti V., Ceserani V., Navone S. E., Falchetti M. L., Parati E. A., Alessandri G., Immortalization of human adipose-derived stromal cells: production of cell lines with high growth rate, mesenchymal marker expression and capability to secrete high levels of angiogenic factors. *Stem Cell Res. Ther.*, 5 (2014) 63.

[41] Mori T., Kiyono T., Imabayashi H., Takeda Y., Tsuchiya K., Miyoshi S., Makino H., Matsumoto K., Saito H., Ogawa S., Sakamoto M., Hata J., Umezawa A., Combination of hTERT and bmi-1, E6, or E7 induces prolongation of the life span of bone marrow stromal cells from an elderly donor without affecting their neurogenic potential. *Mol. Cell. Biol.*, 25 (2005) 5183-5195.
[42] Salazar F., Hall L., Negm O. H., Awuah D., Tighe P. J., Shakib F., Ghaemmaghami A. M., The mannose receptor negatively modulates the Toll-like receptor 4–aryl hydrocarbon receptor–indoleamine 2,3-dioxygenase axis in dendritic cells affecting T helper cell polarization. *J. Allergy Clin. Immunol.*, 137 (2016) 1841-1851.
[43] Carpenter A. E., Jones T. R., Lamprecht M. R., Clarke C., Kang I. H., Friman O., Guertin D. A., Chang J. H., Lindquist R. A., Moffat J., Golland P., Sabatini D. M., CellProfiler: Image Analysis Software for Identifying and Quantifying Cell Phenotypes. *Genome Biology*, 7 (2006) R100.
[44] Everitt B.S., Landau S., Leese M., Cluster Analysis (Fourth ed.), 2001.
[45] Nair D. P., Cramer N. B., Scott T. F., Bowman C. N., Shandas R., Photopolymerized thiol-ene systems as shape memory polymers. *Polymer (Guildf)*, 51 (2010) 4383-4389.
[46] Rutkovskiy A., Stensløkken K. O., Vaage I. J., Osteoblast Differentiation at a Glance. *Med. Sci. Monit. Basic Res.*, 22 (2016) 95-106.
[47] Breiman L., Random Forests. *Mach. Learn.*, 45 (2001) 5-32.
[48] Mikulskis P., Alexander M. R., Winkler D. A., Toward Interpretable Machine Learning Models for Materials Discovery. *Adv. Intel. Syst.*, 1 (2019) 190045.

Figures

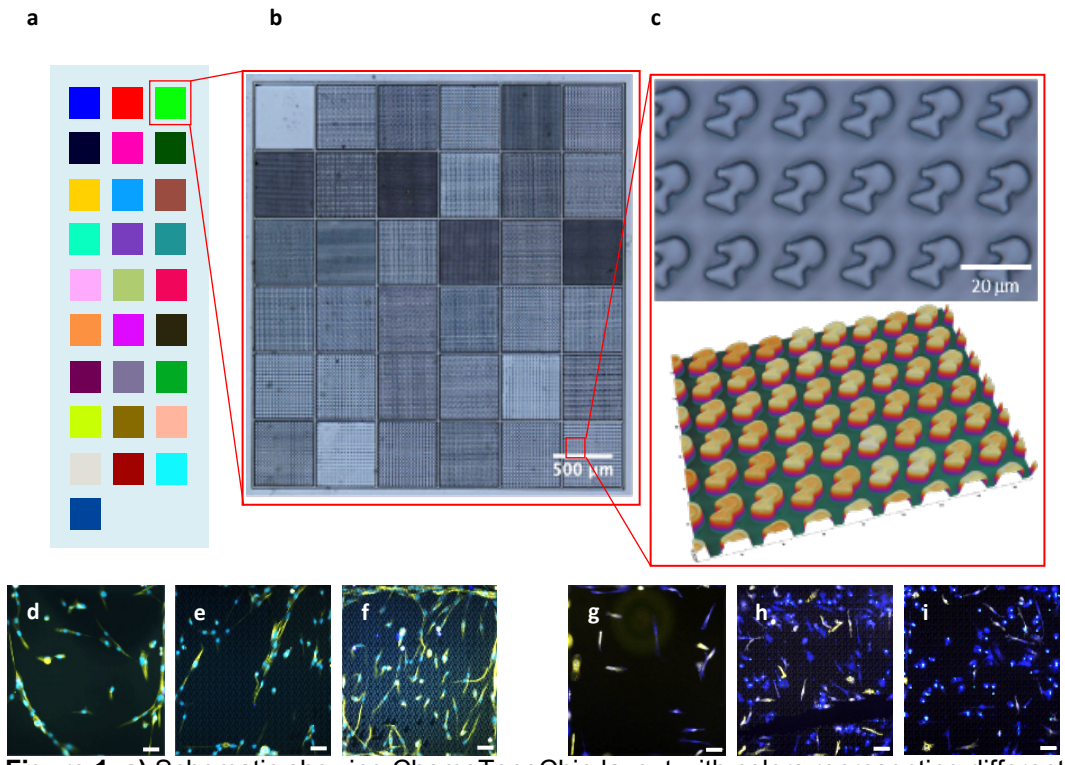

Figure 1. a) Schematic showing ChemoTopoChip layout with colors representing different chemistries; **b)** Interference profilometer imaged ChemoTopo unit (30 µm high walls separate each Topo unit); **c)** Example features from a ChemoTopo unit; hiMSCs (blue = ALP, yellow = α-tubulin); on **d)** flat TMPMP-co-TEGDA area **e)** TMPMP-co-TEGDA + Topo 3 area; **f)** mMAOES + Topo 3 area; Macrophages (blue = IL-10, yellow = TNFα) on **g)** flat TMPMP-co-TEGDA area; **h)** TMPMP-co-TEGDA + Topo 22 area; **i)** BzHPEA + Topo 22 area.

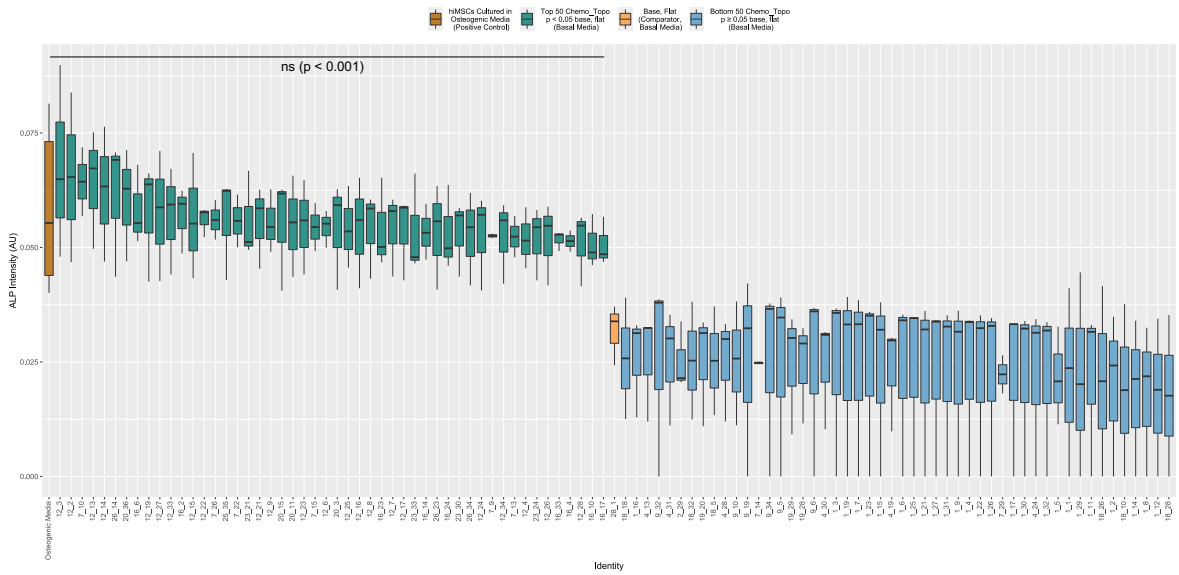

Figure 2. Raw ALP Intensities of hiMSCs cultured on the top 50 ChemoTopo combinations ($p < 0.05$) and bottom 50 ChemoTopo combinations ($p \geq 0.05$) compared to flat base TPMP-co-TEGDA region in basal media, and hiMSCS cultured in osteogenic media.

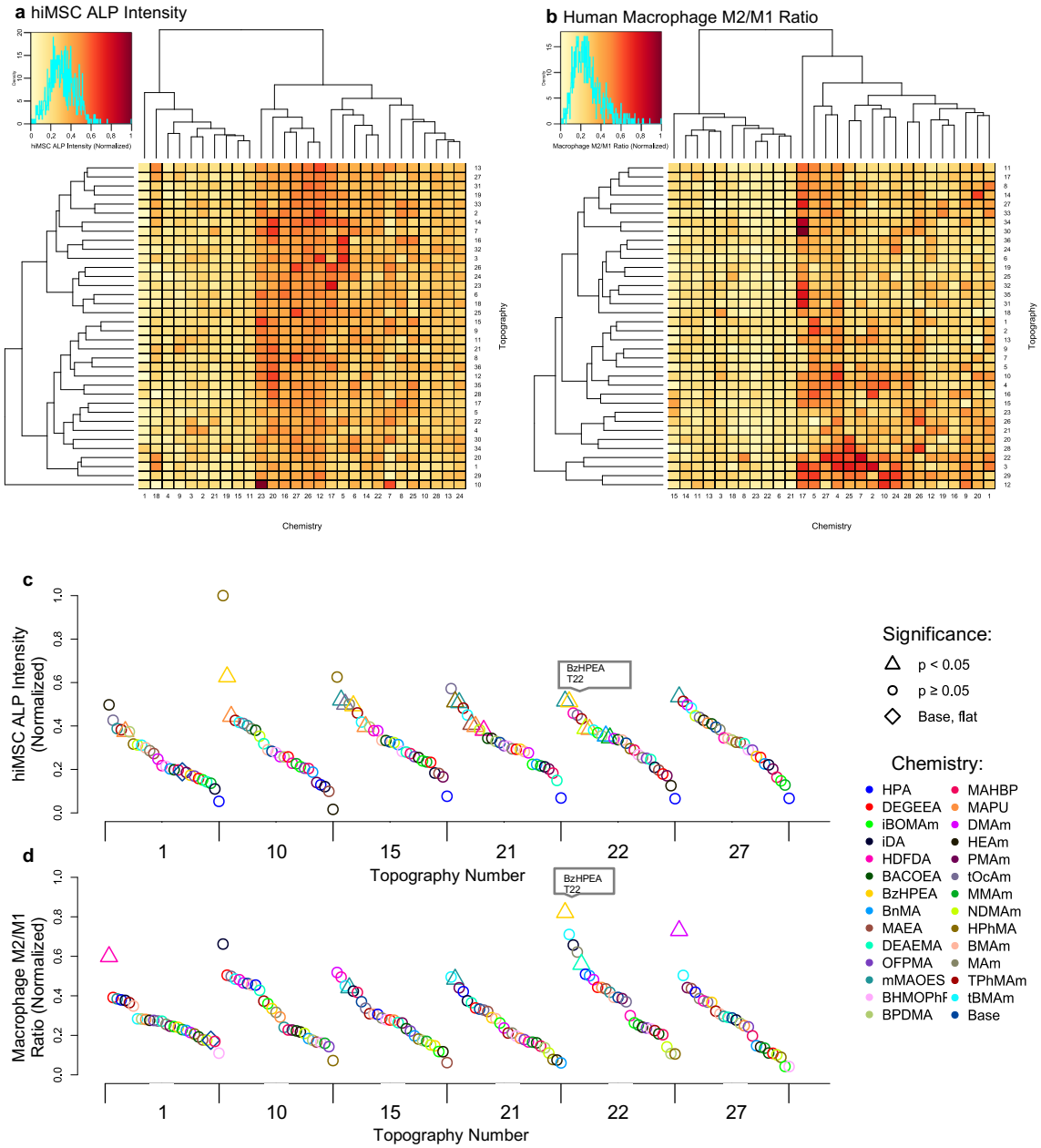

Figure 3. Clustered heatmaps showing **a)** Mean integrated hiMSC ALP expression and **b)** Macrophage M2/M1 ratio across ChemoTopoChip; Rank ordered scatter plots of selected example topographies across all chemistries, showing **c)** Rank hiMSC ALP intensities across the ChemoTopoChip (N = 3, n = 3, see **Figure S8 b** for full ranked plot) and **d)** Rank macrophage M2/M1 ratio across the ChemoTopoChip (N = 2, n = 3, see **Figure S8 d** for full ranked plot). In both scatter plots, t-tests are carried out comparing each data point with the base, flat region and statistical significance is donated by triangular symbols ($p < 0.05$); chemistry is donated by color of plot point.

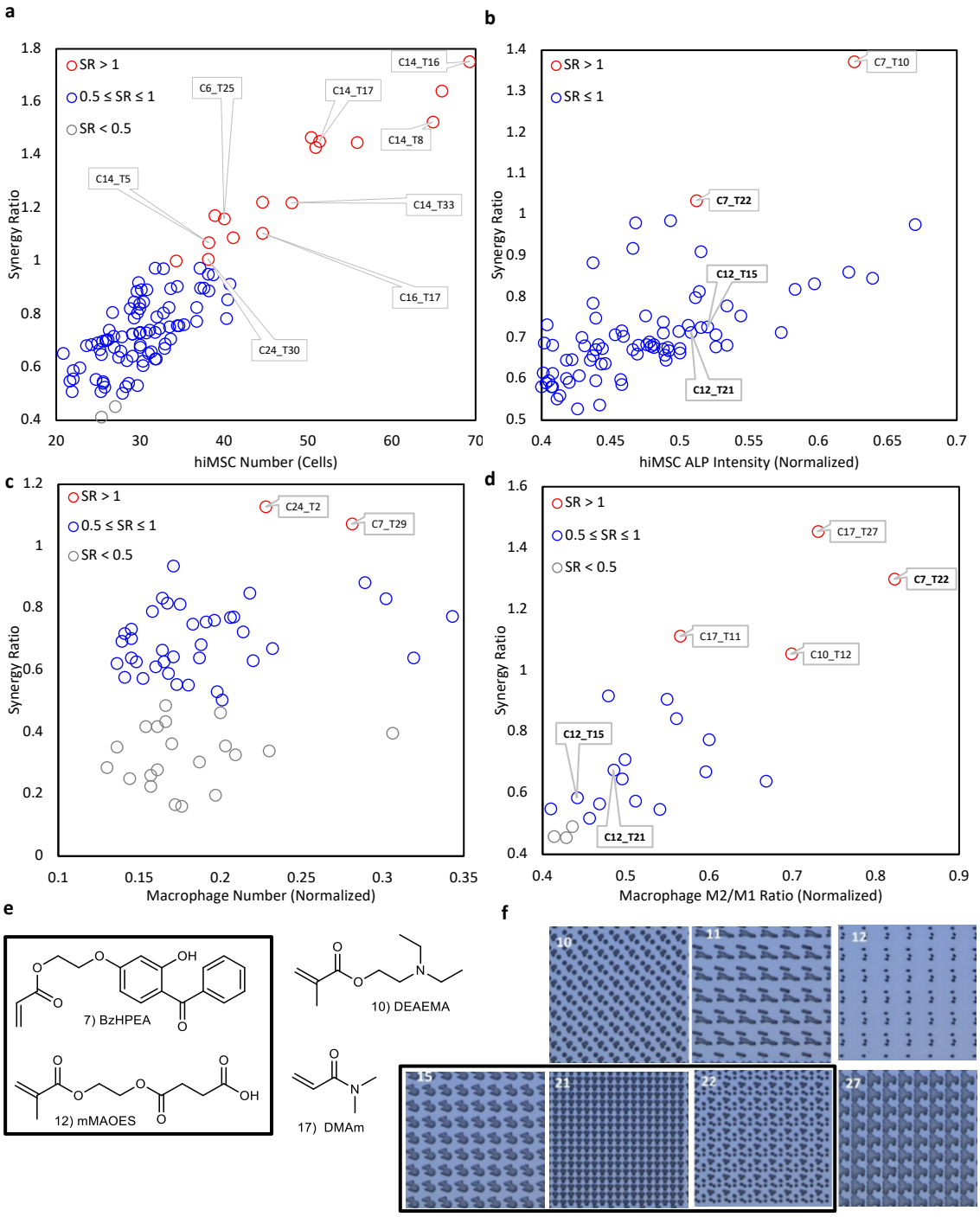

Figure 4. a) *SR* plotted versus hiMSC cell number; **b)** *SR* plotted versus hiMSC ALP intensity (normalized); **c)** *SR* plotted versus human macrophage normalized cell number; **d)** *SR* plotted versus human macrophage M2/M1 ratio (normalized); **e)** Selected hit chemistries from macrophage and hiMSC datasets (see **Figure S2** for full list of chemistries). Coincident M2/M1 and ALP hits highlighted in bold; **f)** Selected hit topographies from macrophage and hiMSC datasets (see **Figure S1** for full list of topographies). Coincident M2/M1 and ALP hits highlighted in bold. See **Table S2 and S3** for full analysis of all synergistic combinations.

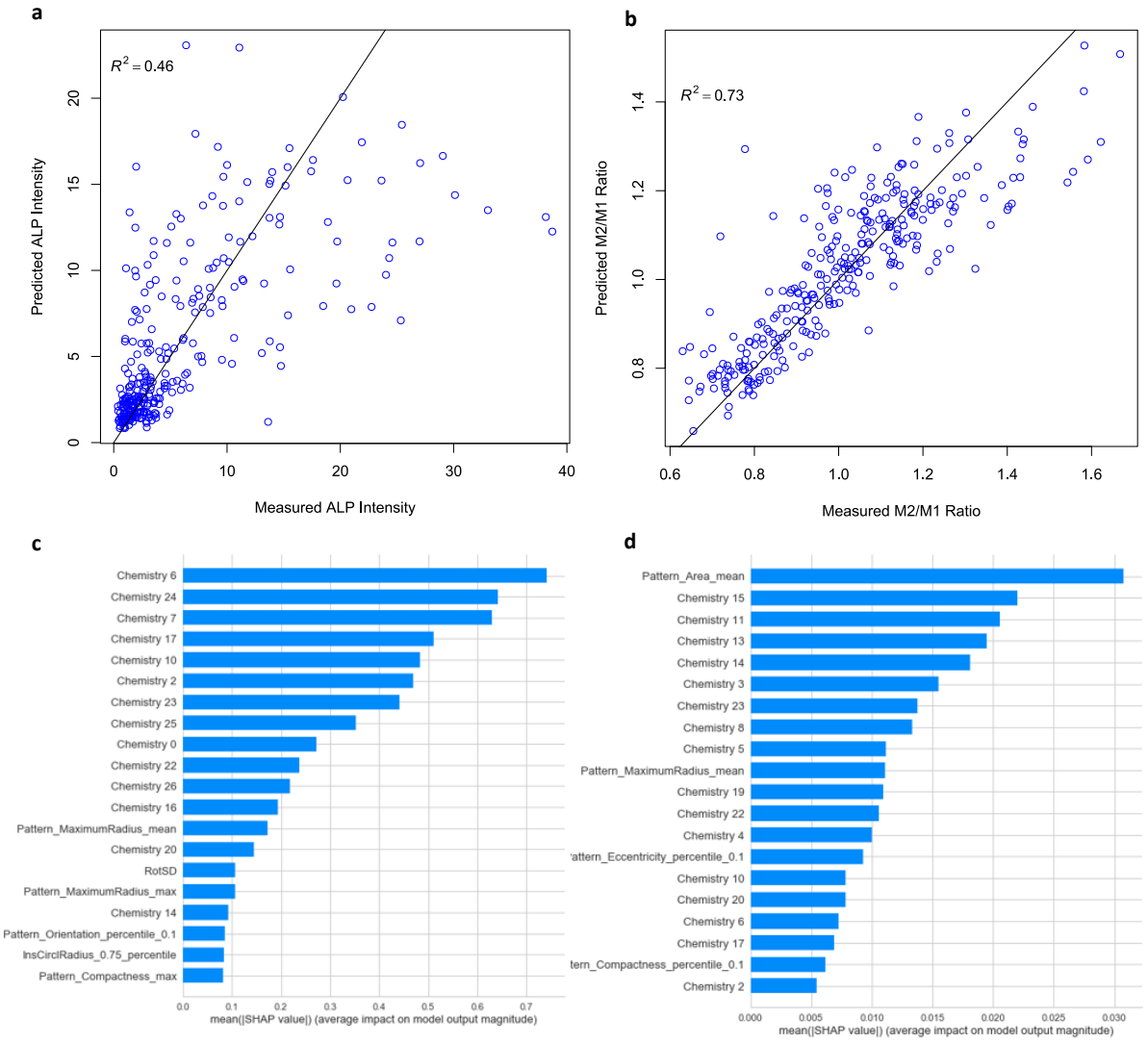

Figure 5. Scatter plots showing **a)** hiMSC ALP intensity random forest model using indicator variables for chemistries and topographical descriptors and **b)** human macrophage polarization random forest model using indicator variables for chemistries and topographical descriptors, line shown is ideal y = x and R^2 corresponds to goodness of fit; **c)** hiMSC ALP intensity random forest model top contributions; **d)** human macrophage polarization random forest model top contributions

Supplementary Data for

Synergistic Material-Topography Combinations to Achieve Immunomodulatory Osteogenic Biomaterials.

Laurence Burroughs, Mahetab H. Amer, Matthew Vassey, Britta Koch, Grazziela P Figueredo, Blessing Mukonoweshuro, Paulius Mikulskis, Aliaksei Vasilevich, Steven Vermeulen, Ian L. Dryden, David A. Winkler, Amir M. Ghaemmaghami, Felicity R. A. J. Rose, Jan de Boer§ and Morgan R. Alexander§*

§ Joint senior authors

* Corresponding Author: Morgan Alexander

Email: morgan.alexander@nottingham.ac.uk

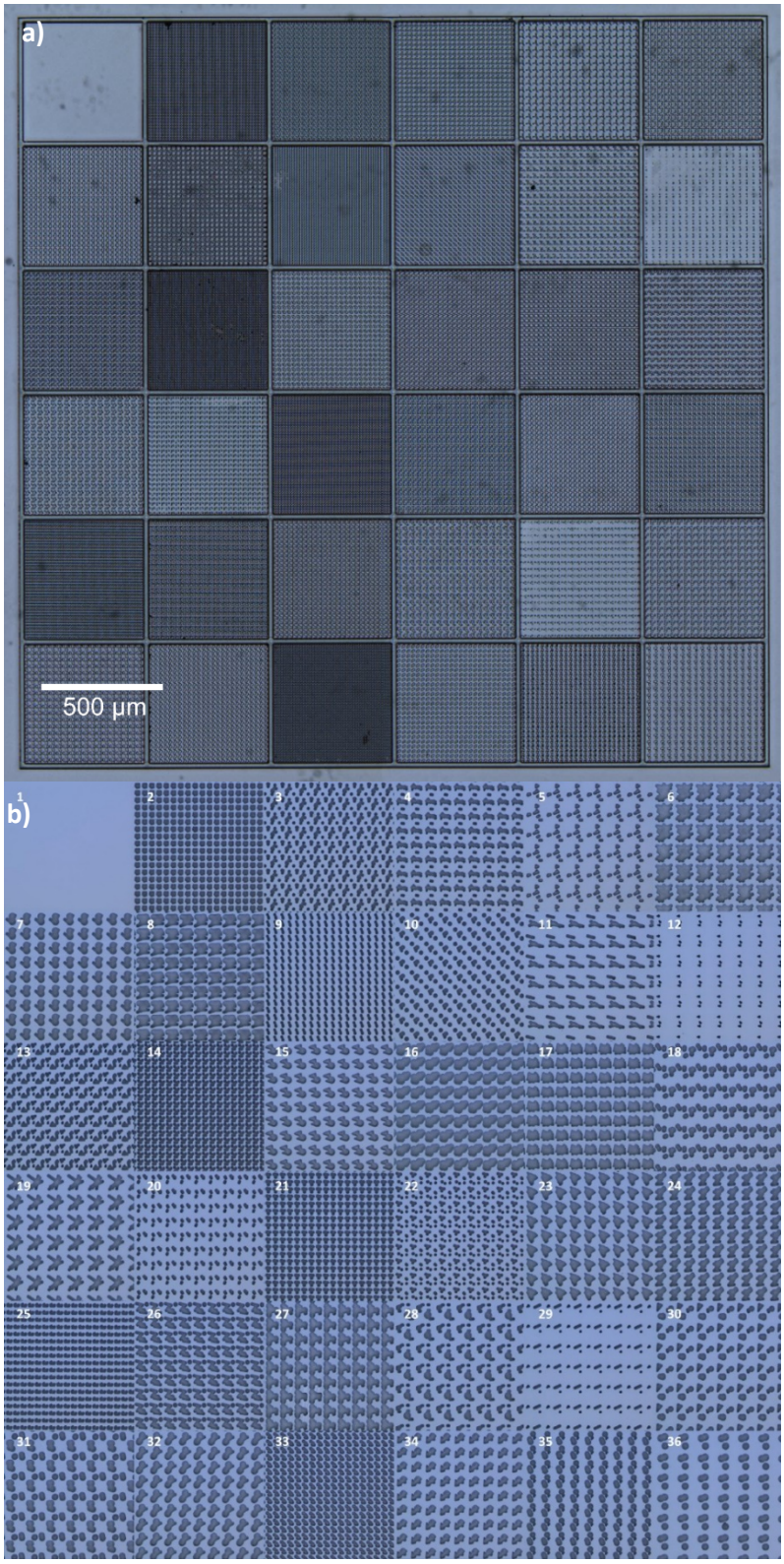

Figure S1 a) Optical profiler image of ChemoTopoChip b) Images of topography shapes

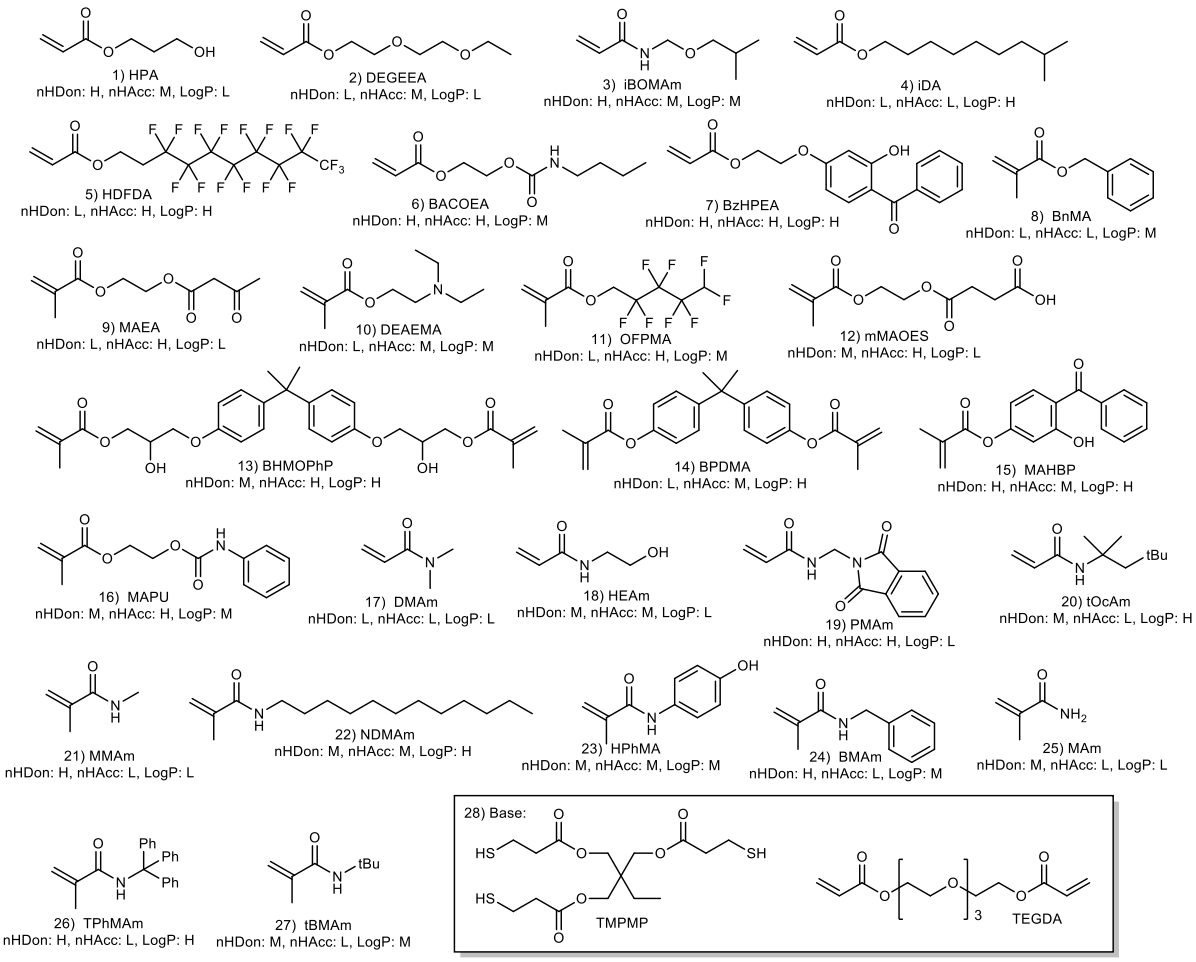

Figure S2 Chemistries Used in the ChemoTopoChip: nHDon, nHAcc and LogP refer to number of H-bond donors, number of H-bond acceptors and LogP (octanol/water partition coefficient) classified as high (H), medium (M) or low (L)

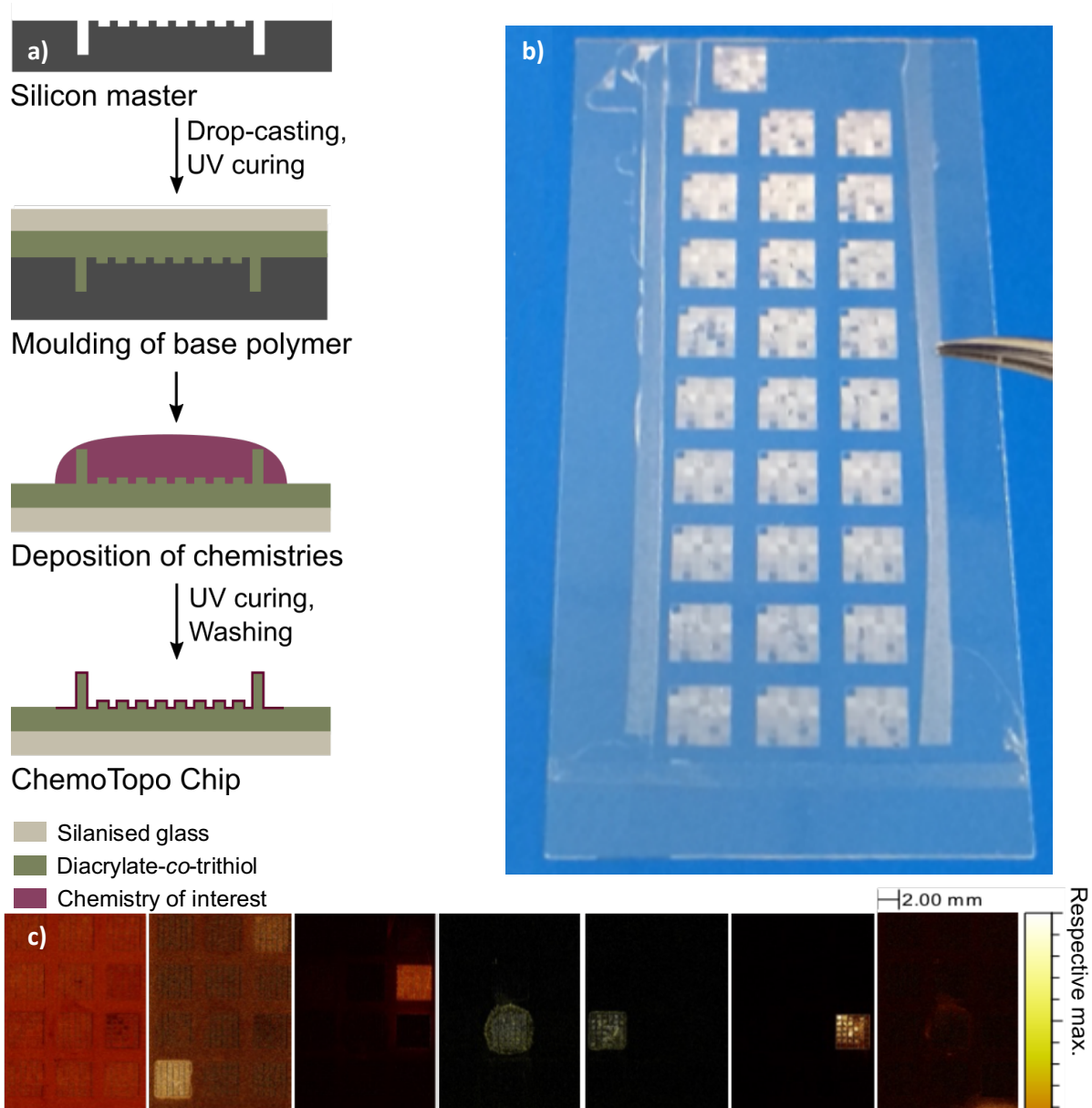

Figure S3 ChemoTopoChip Manufacture

a) ChemoTopoChip production process; **b)** Photographed ChemoTopoChip; **c)** ToF-SIMS images of functionalized surface showing the distribution of the thiol ion from the base and of 6 ions unique to specific functionalization chemistries.

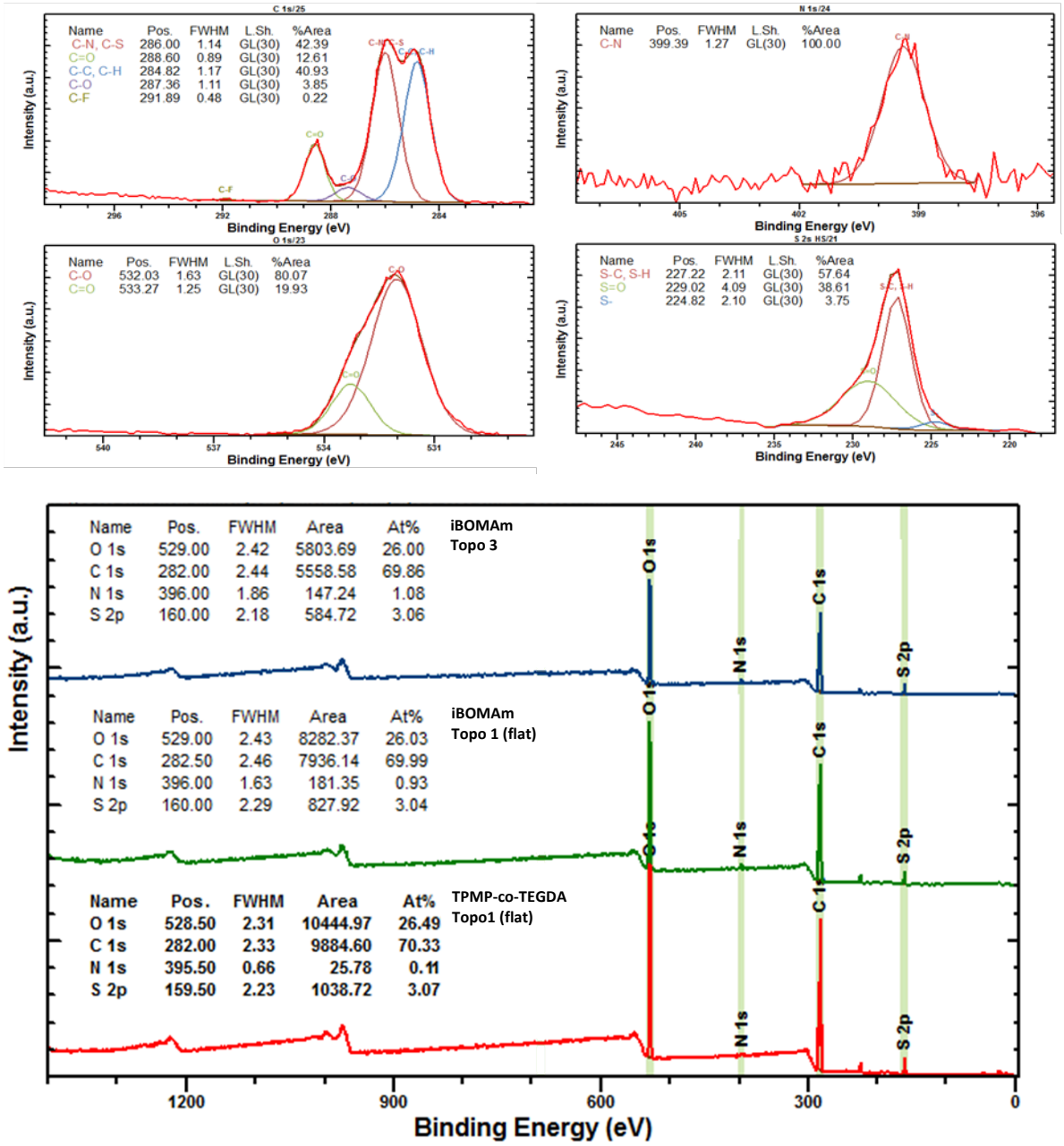

Figure S4 XPS of Base TMPMP-co-TEGDA and Example iBOMAm Functionalized Area

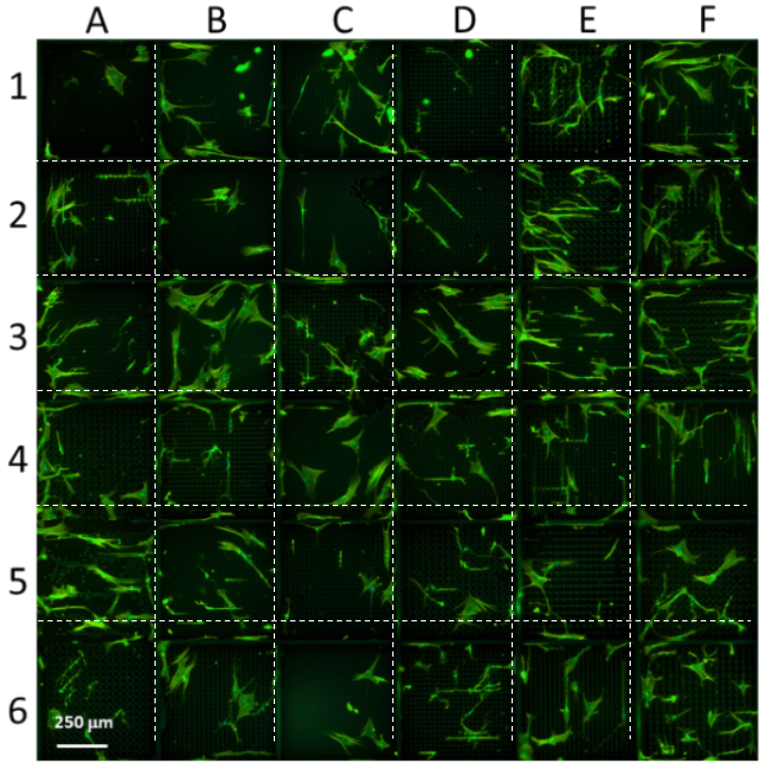

Figure S5 hiMSCs on TMPMP-co-TEGDA ChemoTopo unit, stained with α-tubulin

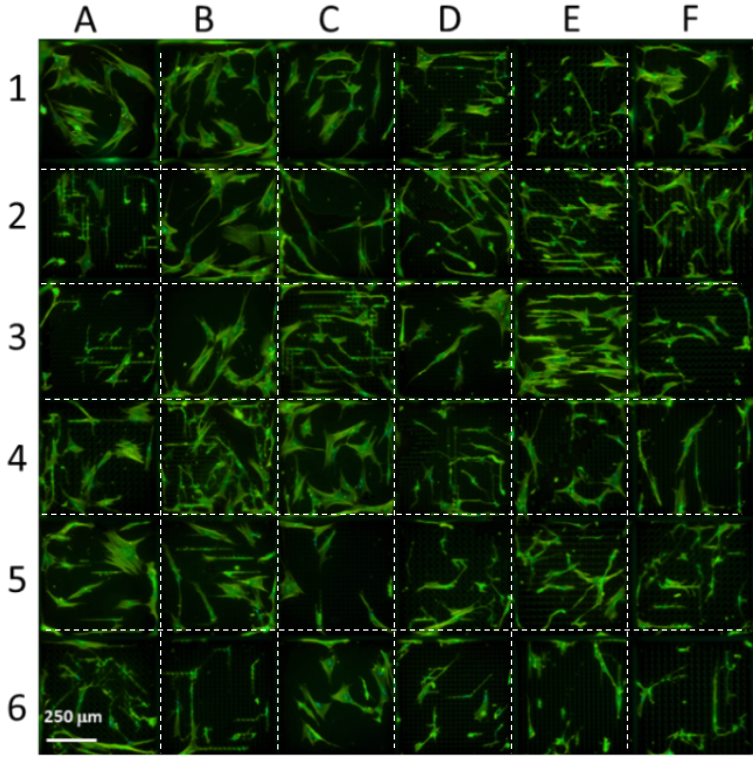

Figure S6 hiMSCs on iBOMAm ChemoTopo unit, stained with α-tubulin

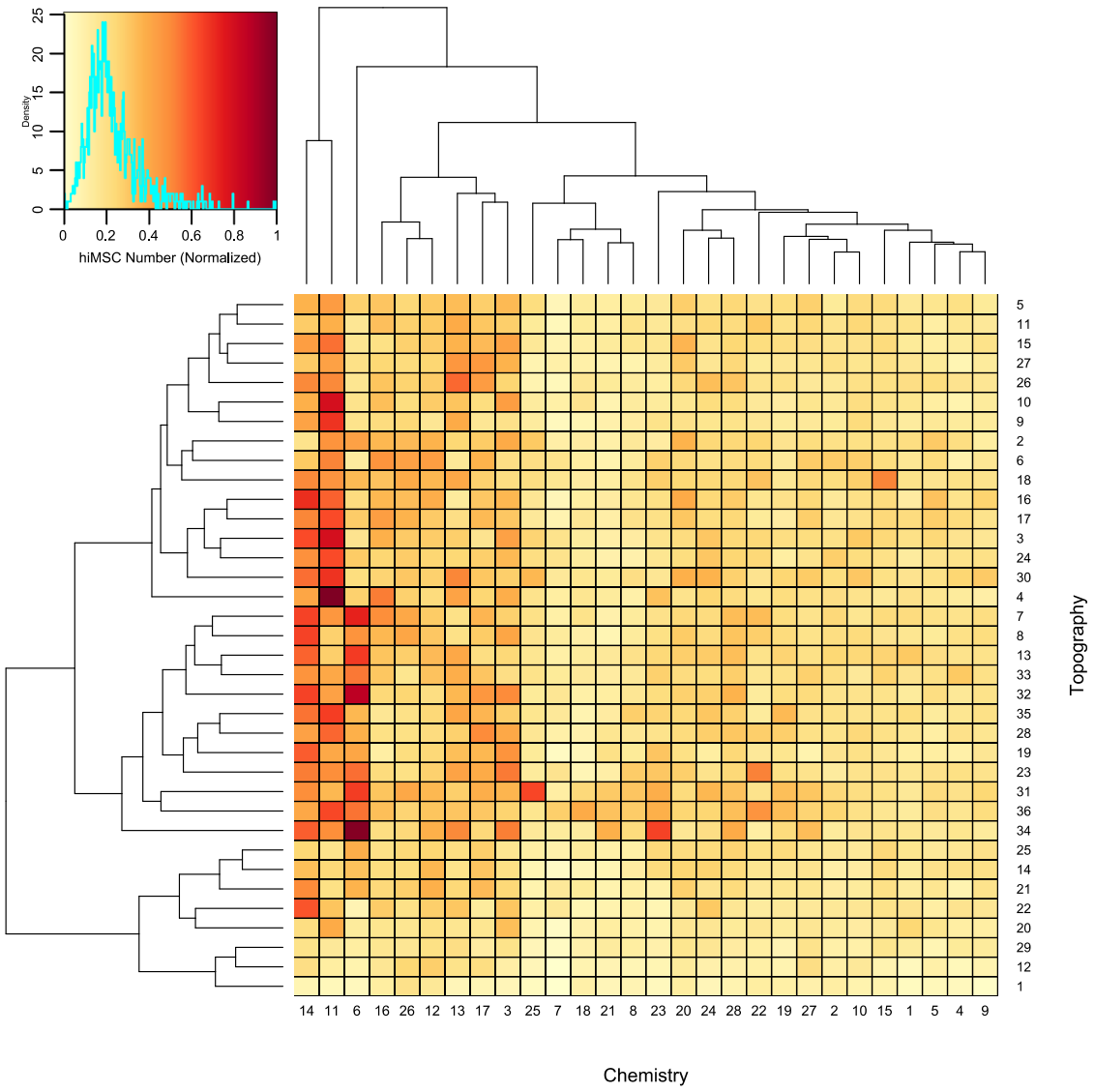

Figure S7 Normalized hiMSC Number Across ChemoTopoChip

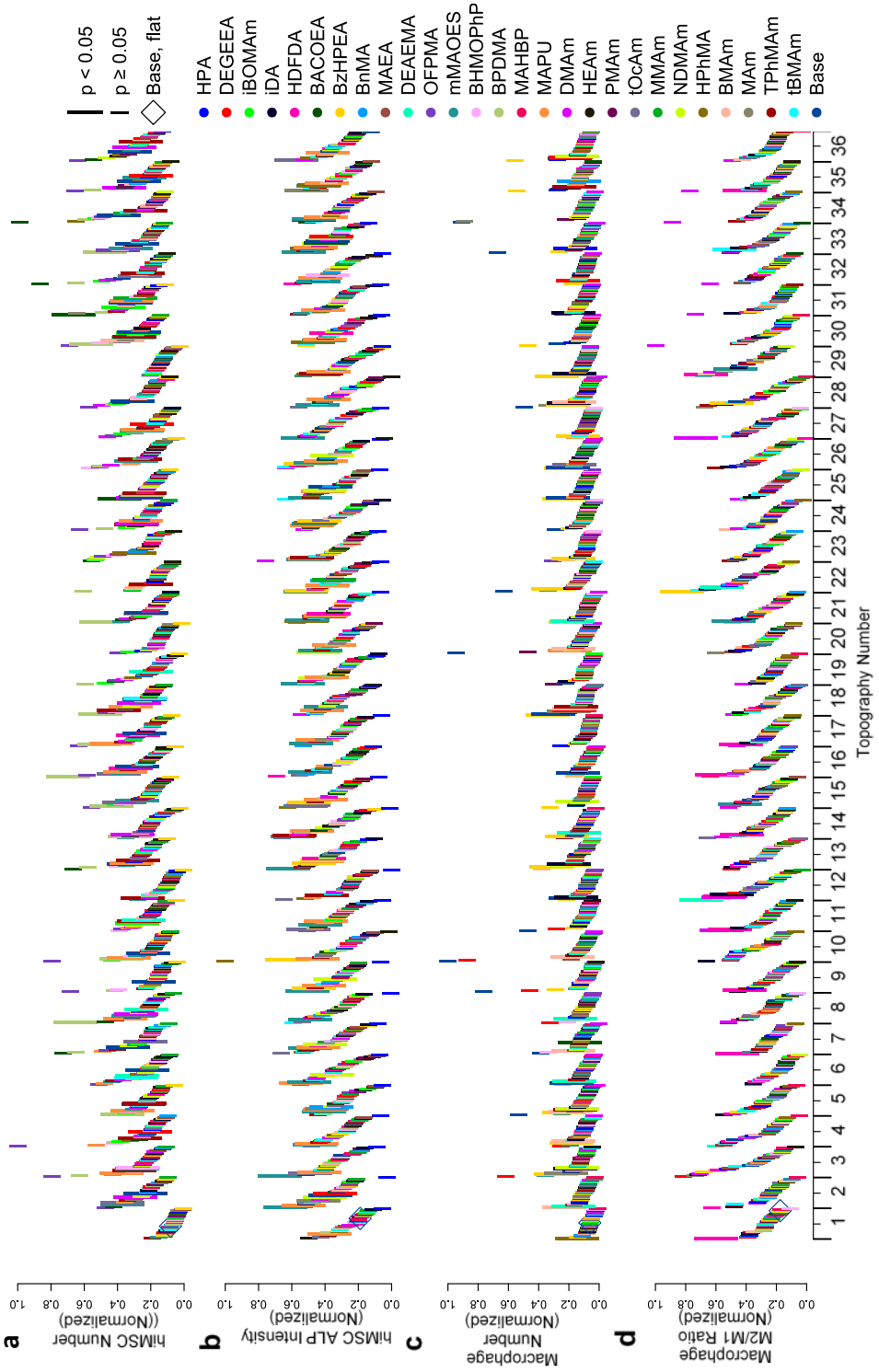

Figure S8 Rank ordered a) hiMSC cell number (N = 3, n = 3) b) hiMSC ALP intensities (N = 3, n = 3) c) human macrophage cell number (N = 2, n = 3) and d) human macrophage M2/M1 ratio (N = 2, n = 3) normalized to flat TMPMP-co-TEGDA area on each ChemoTopoChip

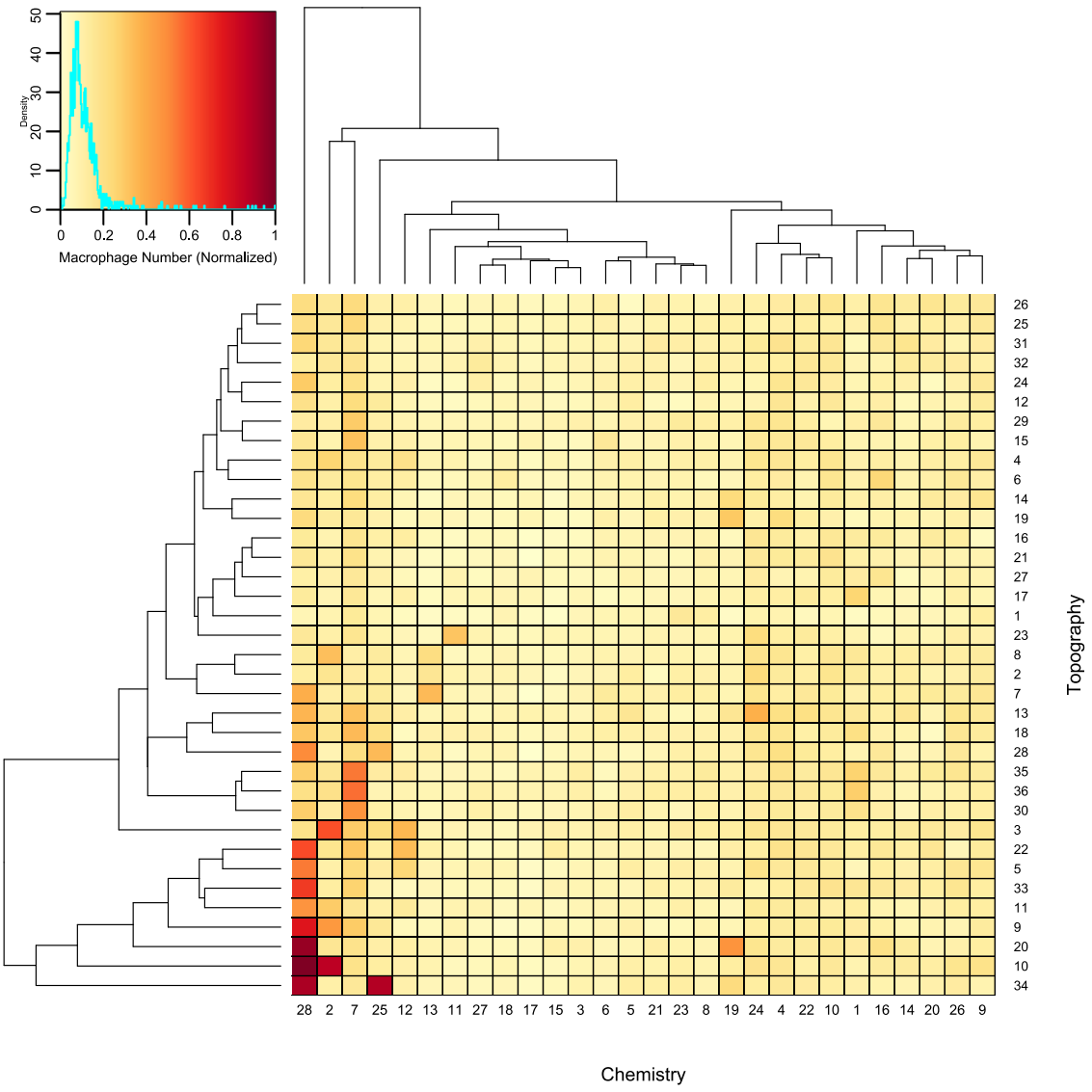

Figure S9 Normalized Macrophage Number Across ChemoTopoChip

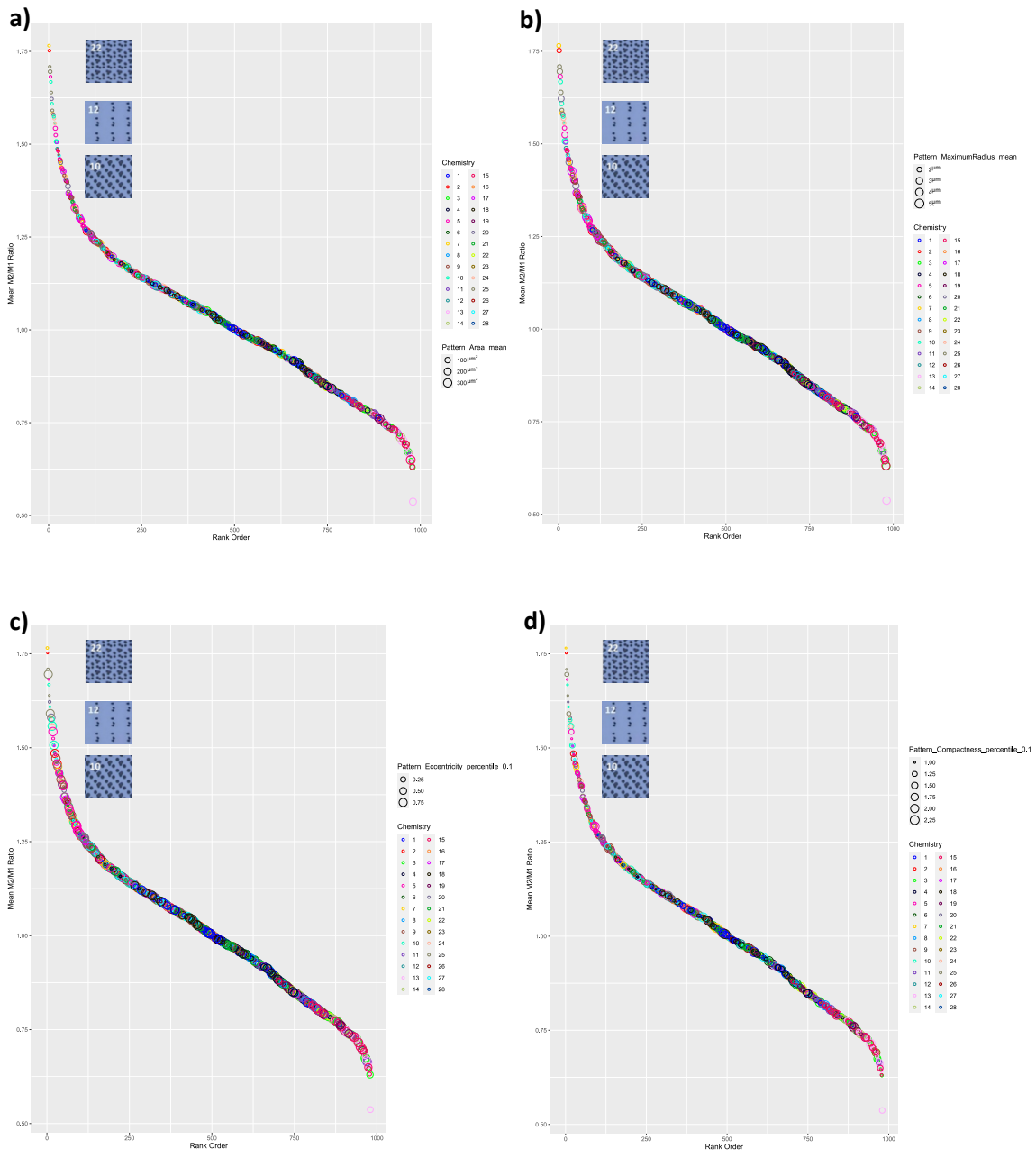

Figure S10 Human Macrophage M2/M1 Ratio Topographical Descriptor Correlation Plots

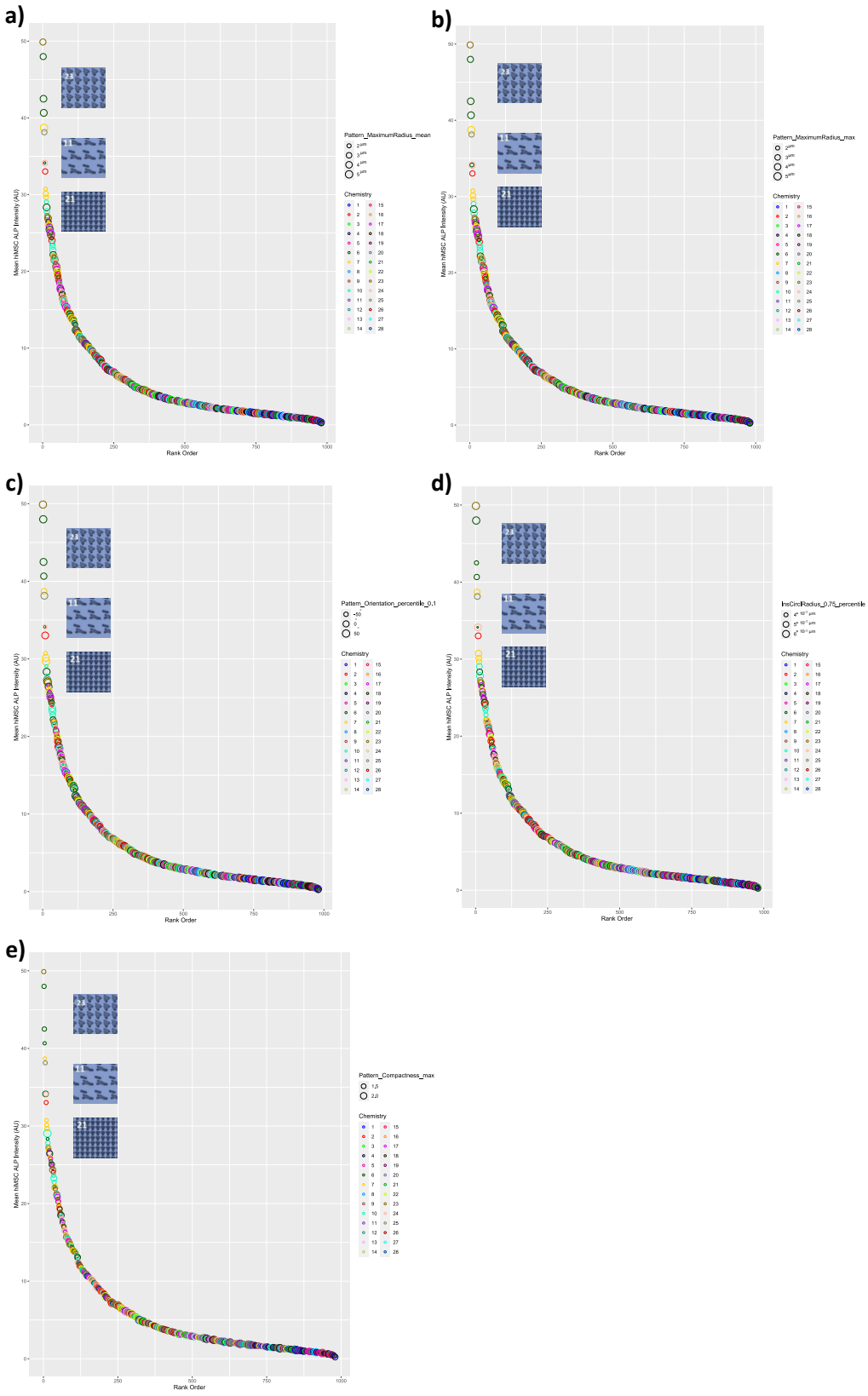

Figure S11 hiMSC ALP Intensity Topographical Descriptor Correlation Plots

Table S1 AFM Modulus data taken from 4 ROIs (t-test comparison with TPMP-co-TEGDA):

Chemistry	Modulus A (MPa)	Modulus B (MPa)	Modulus C (MPa)	Modulus D (MPa)	Mean Modulus (MPa)	Standard Deviation (MPa)	p-value
HPA	110	120	110	110	112	4.33	0.31
DEGEEA	112	117	125	105	115	7.29	0.63
iBOMAm	111	122	118	108	115	5.54	0.59
iDA	126	110	107	127	117	9.07	0.96
HDFDA	105	117	106	115	111	5.31	0.24
BACOEA	117	109	118	108	113	4.53	0.36
BzHPEA	109	127	108	109	113	7.95	0.50
BnMA	70.7	119	119	67.5	94.1	25.0	0.17
MAEA	139	84.4	136	135	124	22.7	0.68
DEAEMA	129	107	121	108	116	9.20	0.84
OFPMA	116	106	111	115	112	3.94	0.29
mMAOES	99.0	109	98.1	118	106	8.13	0.12
BHMOPhP	101	98.1	118	98.2	104	8.27	0.06
BPDMA	122	120	137	104	121	11.7	0.72
MAHBP	106	118	104	108	109	5.39	0.13
MAPU	131	131	101	130	123	12.9	0.53
DMAm	128	101	128	111	117	11.6	0.96
HEAm	105	114	103	104	106	4.39	0.06
PMAm	114	111	112	112	112	1.09	0.23
tOcAm	133	138	96.4	103	117	18.1	0.98
MNAm	107	112	105	107	108	2.59	0.07
NDMAm	102	119	116	112	113	6.42	0.38
HPhMA	120	76.7	106	75.7	94.5	19.1	0.09
BMAm	104	113	108	102	107	4.21	0.06
Mam	134	107	91.6	132	116	17.7	0.90
TPhMAm	113	113	113	112	113	0.43	0.27
tBMAm	127	118	103	125	118	9.42	0.96
TMPMP-co-TEGDA	126	108	123	114	118	7.15	1.00

Table S2 Statistically Signification hiMSC Combinations:

Entry	Chemo	Topo	Normalized ALP	Chemo Comparator ALP	Topo Comparator ALP	*SR*	Entry	Chemo	Topo	Cell Count	Chemo Comparator Count	Topo Comparator Count	*SR*
1	mMAOES	3	0.670	0.388	0.297	0.977	1	BPDMA	33	48.1	9.6	29.9	1.220
2	mMAOES	2	0.639	0.388	0.367	0.846	2	TPhMAm	18	40.4	21.2	26.0	0.856
3	BzHPEA	10	0.626	0.173	0.283	1.372	3	MAPU	3	38.7	14.4	26.3	0.948
4	mMAOES	13	0.622	0.388	0.334	0.861	4	BPDMA	14	34.3	9.6	24.7	1.002
5	mMAOES	14	0.597	0.388	0.330	0.832	5	BPDMA	8	64.9	9.6	33.0	1.525
6	TPhMAm	14	0.583	0.383	0.330	0.819	6	BPDMA	18	50.9	9.6	26.0	1.429
7	tOcAm	36	0.573	0.426	0.376	0.714	7	TPhMAm	30	31.8	21.2	29.1	0.632
8	MAPU	6	0.544	0.375	0.347	0.755	8	DMAm	2	30.8	9.0	25.5	0.893
9	mMAOES	19	0.534	0.388	0.298	0.779	9	OFPMA	33	41.1	7.9	29.9	1.088
10	mMAOES	27	0.534	0.388	0.395	0.683	10	DMAm	36	31.8	9.0	34.4	0.733
11	mMAOES	33	0.526	0.388	0.386	0.679	11	mMAOES	8	31.9	17.6	33.0	0.631
12	MAPU	2	0.526	0.375	0.367	0.709	12	tOcAm	2	38.1	14.6	25.5	0.952
13	mMAOES	15	0.520	0.388	0.327	0.727	13	TPhMAm	3	31.3	21.2	26.3	0.659
14	mMAOES	22	0.515	0.388	0.321	0.726	14	MAPU	27	26.9	14.4	25.4	0.675
15	BzHPEA	26	0.515	0.173	0.392	0.910	15	TPhMAm	12	26.7	21.2	11.8	0.807
16	MAm	35	0.514	0.286	0.346	0.813	16	tBMAm	6	30.4	11.8	24.2	0.846
17	BzHPEA	22	0.512	0.173	0.321	1.035	17	Base	33	29.9	11.0	29.9	0.730
18	HPhMA	21	0.511	0.317	0.323	0.799	18	BPDMA	21	50.4	9.6	24.9	1.466
19	mMAOES	21	0.508	0.388	0.323	0.714	19	Base	35	29.1	11.0	29.1	0.725
20	mMAOES	9	0.506	0.388	0.304	0.731	20	tOcAm	15	37.2	14.6	26.9	0.898
21	tOcAm	15	0.500	0.426	0.327	0.664	21	DMAm	18	28.8	9.0	26.0	0.821
22	tOcAm	11	0.500	0.426	0.314	0.675	22	TPhMAm	32	27.0	21.2	38.3	0.453
23	mMAOES	23	0.499	0.388	0.309	0.716	23	MAPU	31	33.0	14.4	33.5	0.688
24	BzHPEA	15	0.493	0.173	0.327	0.986	24	tOcAm	7	25.3	14.6	35.2	0.509
25	mMAOES	6	0.492	0.388	0.347	0.670	25	DEAEMA	6	29.9	11.4	24.2	0.839
26	tOcAm	3	0.491	0.426	0.297	0.678	26	MAPU	5	32.8	14.4	26.2	0.806
27	mMAOES	25	0.490	0.388	0.369	0.647	27	TPhMAm	11	29.1	21.2	24.1	0.642
28	mMAOES	16	0.489	0.388	0.353	0.659	28	HDFDA	16	33.6	7.4	30.0	0.896
29	mMAOES	8	0.488	0.388	0.336	0.674	29	DMAm	14	32.8	9.0	24.7	0.972
30	MAPU	23	0.488	0.375	0.309	0.713	30	Base	16	30.0	11.0	30.0	0.731
31	mMAOES	7	0.488	0.388	0.271	0.740	31	TPhMAm	26	28.3	21.2	32.5	0.527
32	mMAOES	17	0.481	0.388	0.321	0.678	32	DEAEMA	8	24.7	11.4	33.0	0.555
33	HPhMA	33	0.481	0.317	0.386	0.684	33	iBOMAm	30	29.3	8.2	29.1	0.786
34	MAPU	14	0.479	0.375	0.330	0.680	34	Base	36	34.4	11.0	34.4	0.757
35	TPhMAm	23	0.478	0.383	0.309	0.691	35	BPDMA	25	26.8	9.6	27.8	0.717
36	MAPU	24	0.476	0.375	0.321	0.684	36	MAPU	16	36.7	14.4	30.0	0.825

37	HPhMA	30	0.475	0.317	0.313	0.754	37	MAPU	24	27.7	14.4	27.4	0.662
38	TPhMAm	34	0.470	0.383	0.305	0.683	38	Base	30	29.1	11.0	29.1	0.725
39	mMAOES	24	0.469	0.388	0.321	0.662	39	HDFDA	17	29.6	7.4	25.9	0.887
40	BzHPEA	9	0.468	0.173	0.304	0.980	40	BPDMA	30	55.9	9.6	29.1	1.447
41	mMAOES	34	0.466	0.388	0.305	0.672	41	mMAOES	2	38.2	17.6	25.5	0.888
42	BzHPEA	13	0.466	0.173	0.334	0.918	42	DEAEMA	11	26.3	11.4	24.1	0.740
43	mMAOES	4	0.459	0.388	0.264	0.705	43	BPDMA	10	38.9	9.6	23.6	1.172
44	HPhMA	24	0.458	0.317	0.321	0.718	44	Base	6	24.2	11.0	24.2	0.687
45	mMAOES	26	0.458	0.388	0.392	0.587	45	MMAm	31	31.1	8.4	33.5	0.741
46	MAPU	33	0.457	0.375	0.386	0.600	46	MAPU	13	32.9	14.4	34.6	0.671
47	MAPU	4	0.453	0.375	0.264	0.709	47	DEGEEA	4	22.8	13.9	24.2	0.598
48	mMAOES	28	0.446	0.388	0.311	0.639	48	HPhMA	23	31.8	7.0	25.6	0.974
49	MAPU	10	0.444	0.375	0.283	0.675	49	mMAOES	3	30.0	17.6	26.3	0.684
50	MAPU	17	0.443	0.375	0.321	0.637	50	Base	13	34.6	11.0	34.6	0.758
51	mMAOES	32	0.442	0.388	0.432	0.538	51	TPhMAm	36	27.9	21.2	34.4	0.502
52	MAPU	7	0.441	0.375	0.271	0.684	52	MAPU	17	44.6	14.4	25.9	1.105
53	MAm	2	0.439	0.286	0.367	0.672	53	tOcAm	16	40.7	14.6	30.0	0.913
54	HPhMA	29	0.439	0.317	0.270	0.749	54	BMAm	30	38.1	8.8	29.1	1.007
55	mMAOES	35	0.439	0.388	0.346	0.597	55	Base	31	33.5	11.0	33.5	0.752
56	NDMAm	20	0.437	0.313	0.244	0.785	56	tOcAm	8	31.0	14.6	33.0	0.652
57	BzHPEA	24	0.437	0.173	0.321	0.883	57	Base	18	26.0	11.0	26.0	0.702
58	HPhMA	35	0.437	0.317	0.346	0.658	58	Base	17	25.9	11.0	25.9	0.701
59	MAPU	3	0.435	0.375	0.297	0.647	59	Base	5	26.2	11.0	26.2	0.704
60	mMAOES	20	0.431	0.388	0.244	0.682	60	DMAm	25	29.7	9.0	27.8	0.806
61	NDMAm	19	0.429	0.313	0.298	0.702	61	mMAOES	27	27.4	17.6	25.4	0.639
62	mMAOES	11	0.427	0.388	0.314	0.609	62	MAPU	18	33.4	14.4	26.0	0.826
63	MAPU	32	0.426	0.375	0.432	0.528	63	TPhMAm	4	28.4	21.2	24.2	0.626
64	TPhMAm	29	0.422	0.383	0.270	0.648	64	TPhMAm	22	22.0	21.2	18.4	0.556
65	MAPU	13	0.420	0.375	0.334	0.593	65	MAPU	21	25.4	14.4	24.9	0.648
66	NDMAm	13	0.418	0.313	0.334	0.647	66	TPhMAm	13	29.7	21.2	34.6	0.532
67	MAPU	18	0.418	0.375	0.319	0.602	67	Base	25	27.8	11.0	27.8	0.716
68	MAPU	31	0.413	0.375	0.362	0.561	68	DMAm	8	30.7	9.0	33.0	0.730
69	MAPU	25	0.411	0.375	0.369	0.552	69	TPhMAm	5	25.6	21.2	26.2	0.539
70	mMAOES	5	0.408	0.388	0.277	0.614	70	BHMOPhP	3	29.3	8.3	26.3	0.846
71	mMAOES	30	0.408	0.388	0.313	0.582	71	iBOMAm	11	29.8	8.2	24.1	0.920
72	MAEA	21	0.408	0.273	0.323	0.683	72	BPDMA	11	30.1	9.6	24.1	0.893
73	NDMAm	33	0.407	0.313	0.386	0.582	73	DMAm	24	29.9	9.0	27.4	0.822
74	MAPU	9	0.405	0.375	0.304	0.597	74	iBOMAm	31	37.6	8.2	33.5	0.899
75	HDFDA	13	0.404	0.218	0.334	0.733	75	MAPU	8	36.7	14.4	33.0	0.773

76	NDMAm	2	0.403	0.313	0.367	0.592
77	NDMAm	7	0.402	0.313	0.271	0.689
78	MAPU	5	0.401	0.375	0.277	0.615
79	MAPU	30	0.400	0.375	0.313	0.582
80	NDMAm	25	0.398	0.313	0.369	0.584
81	MAPU	26	0.398	0.375	0.392	0.519
82	MAPU	21	0.398	0.375	0.323	0.570
83	MAPU	15	0.398	0.375	0.327	0.567
84	MAPU	34	0.396	0.375	0.305	0.583
85	MAPU	11	0.396	0.375	0.314	0.575
86	BACOEA	33	0.396	0.199	0.386	0.677
87	mMAOES	18	0.396	0.388	0.319	0.559
88	MAm	5	0.390	0.286	0.277	0.693
89	MAPU	35	0.390	0.375	0.346	0.541
90	MAPU	19	0.389	0.375	0.298	0.579
91	TPhMAm	12	0.389	0.383	0.243	0.621
92	NDMAm	22	0.389	0.313	0.321	0.613
93	#N/A	33	0.386	0.189	0.386	0.672
94	MAPU	36	0.385	0.375	0.376	0.513
95	MAPU	22	0.385	0.375	0.321	0.553
96	BHMOPhP	32	0.383	0.214	0.432	0.593
97	HDFDA	21	0.380	0.218	0.323	0.703
98	MAPU	28	0.380	0.375	0.311	0.554
99	MAPU	29	0.378	0.375	0.270	0.587
100	MAPU	1	0.375	0.375	0.189	0.665
101	BPDMA	33	0.370	0.373	0.386	0.487
102	#N/A	25	0.369	0.189	0.369	0.662
103	#N/A	2	0.367	0.189	0.367	0.660
104	BnMA	5	0.363	0.202	0.277	0.758
105	DEGEEA	33	0.362	0.159	0.386	0.665
106	HDFDA	30	0.361	0.218	0.313	0.680
107	NDMAm	6	0.357	0.313	0.347	0.542
108	NDMAm	26	0.355	0.313	0.392	0.504
109	BnMA	22	0.354	0.202	0.321	0.677
110	MAPU	20	0.347	0.375	0.244	0.561
111	MMAm	22	0.345	0.136	0.321	0.756
112	NDMAm	9	0.342	0.313	0.304	0.555
113	DEGEEA	2	0.339	0.159	0.367	0.646

76	BPDMA	5	38.2	9.6	26.2	1.069
77	Base	10	23.6	11.0	23.6	0.682
78	Base	34	40.3	11.0	40.3	0.785
79	DEAEMA	30	32.0	11.4	29.1	0.790
80	MAPU	10	34.4	14.4	23.6	0.905
81	Base	21	24.9	11.0	24.9	0.692
82	Base	2	25.5	11.0	25.5	0.698
83	tBMAm	18	25.2	11.8	26.0	0.667
84	DEGEEA	27	21.6	13.9	25.4	0.549
85	DEAEMA	19	22.0	11.4	26.1	0.587
86	BPDMA	17	51.4	9.6	25.9	1.452
87	tOcAm	32	28.6	14.6	38.3	0.540
88	BPDMA	15	44.6	9.6	26.9	1.223
89	Base	9	20.8	11.0	20.8	0.653
90	mMAOES	33	33.6	17.6	29.9	0.707
91	mMAOES	26	30.3	17.6	32.5	0.606
92	DMAm	35	37.1	9.0	29.1	0.973
93	BACOEA	31	66.0	6.7	33.5	1.642
94	mMAOES	35	25.6	17.6	29.1	0.547
95	TPhMAm	34	25.4	21.2	40.3	0.413
96	DEGEEA	35	21.9	13.9	29.1	0.509
97	Base	7	35.2	11.0	35.2	0.762
98	BACOEA	25	40.0	6.7	27.8	1.160
99	TPhMAm	24	30.3	21.2	27.4	0.624
100	BPDMA	16	69.3	9.6	30.0	1.753
101	mMAOES	15	30.0	17.6	26.9	0.675
102	Base	28	32.3	11.0	32.3	0.746
103	TPhMAm	25	25.8	21.2	27.8	0.526

Table S3 Statistically Significant Macrophage Combinations:

Entry	Chemo	Topo	Normalized M2/M1	Chemo Comparator M2/M1	Topo Comparator M2/M1	*SR*
1	7	22	0.822	0.240	0.392	1.299
2	17	27	0.730	0.214	0.288	1.454
3	10	12	0.698	0.272	0.391	1.054
4	5	29	0.668	0.599	0.446	0.639
5	5	1	0.599	0.599	0.175	0.774
6	5	16	0.595	0.599	0.289	0.670
7	17	11	0.565	0.214	0.293	1.112
8	10	22	0.560	0.272	0.392	0.843
9	17	12	0.549	0.214	0.391	0.907
10	5	12	0.540	0.599	0.391	0.546
11	5	11	0.511	0.599	0.293	0.573
12	7	28	0.498	0.240	0.462	0.710
13	4	12	0.495	0.377	0.391	0.646
14	12	21	0.485	0.385	0.333	0.675
15	27	33	0.478	0.284	0.237	0.918
16	12	29	0.468	0.385	0.446	0.564
17	5	7	0.456	0.599	0.281	0.518
18	12	15	0.441	0.385	0.370	0.585
19	5	17	0.435	0.599	0.287	0.491
20	5	14	0.428	0.599	0.343	0.455
21	5	9	0.413	0.599	0.301	0.459
22	5	35	0.409	0.599	0.148	0.548

Entry	Chemo	Topo	Normalized Count	Chemo Comparator Count	Topo Comparator Count	*SR*
1	23	1	0.145	0.145	0.061	0.703
2	24	10	0.176	0.082	1.000	0.162
3	0	12	0.191	0.061	0.191	0.757
4	4	12	0.152	0.075	0.191	0.574
5	22	13	0.201	0.041	0.358	0.504
6	4	13	0.200	0.075	0.358	0.463
7	7	13	0.319	0.140	0.358	0.640
8	10	14	0.136	0.063	0.156	0.623
9	7	14	0.214	0.140	0.156	0.724
10	22	15	0.145	0.041	0.157	0.733
11	0	16	0.139	0.061	0.139	0.694
12	0	18	0.302	0.061	0.302	0.832
13	2	18	0.166	0.080	0.302	0.435
14	24	18	0.161	0.082	0.302	0.419
15	25	18	0.198	0.070	0.302	0.532
16	26	18	0.154	0.066	0.302	0.418
17	7	18	0.343	0.140	0.302	0.774
18	10	2	0.171	0.063	0.120	0.937
19	24	2	0.228	0.082	0.120	1.128
20	16	20	0.197	0.050	0.949	0.198
21	24	20	0.172	0.082	0.949	0.167
22	10	21	0.175	0.063	0.152	0.813
23	7	21	0.187	0.140	0.152	0.641
24	7	22	0.306	0.140	0.632	0.397
25	7	23	0.168	0.140	0.143	0.591
26	0	25	0.206	0.061	0.206	0.771
27	7	25	0.232	0.140	0.206	0.671
28	0	26	0.208	0.061	0.208	0.772
29	20	26	0.165	0.055	0.208	0.628
30	7	26	0.220	0.140	0.208	0.631
31	7	27	0.141	0.140	0.104	0.577
32	24	28	0.161	0.082	0.496	0.279
33	4	28	0.203	0.075	0.496	0.356
34	7	28	0.209	0.140	0.496	0.328
35	24	29	0.167	0.082	0.122	0.817
36	4	29	0.164	0.075	0.122	0.833

37	7	29	0.281	0.140	0.122	1.072
38	22	3	0.145	0.041	0.186	0.640
39	25	3	0.218	0.070	0.186	0.850
40	4	3	0.160	0.075	0.186	0.612
41	7	3	0.289	0.140	0.186	0.883
42	4	31	0.173	0.075	0.237	0.555
43	2	32	0.141	0.080	0.116	0.719
44	1	33	0.157	0.030	0.670	0.225
45	26	35	0.166	0.066	0.275	0.486
46	8	35	0.136	0.110	0.275	0.353
47	0	36	0.196	0.061	0.196	0.762
48	2	36	0.188	0.080	0.196	0.683
49	22	36	0.148	0.041	0.196	0.627
50	24	4	0.171	0.082	0.184	0.643
51	7	4	0.180	0.140	0.184	0.553
52	22	5	0.144	0.041	0.533	0.251
53	24	5	0.187	0.082	0.533	0.304
54	26	5	0.157	0.066	0.533	0.261
55	7	5	0.230	0.140	0.533	0.341
56	0	6	0.183	0.061	0.183	0.750
57	10	6	0.164	0.063	0.183	0.666
58	24	7	0.170	0.082	0.384	0.364
59	6	7	0.130	0.069	0.384	0.287
60	10	8	0.158	0.063	0.136	0.791

Table S4 Topographical Descriptors:[1]

Basic Shape Feature	Description	Features Highlighted From Model	Description
Eccentricity	The eccentricity of the ellipse that has the same second-moments as the region. The eccentricity is the ratio of the distance between the foci of the ellipse and its major axis length. The value is between 0 and 1. (0 and 1 are degenerate cases; an ellipse whose eccentricity is 0 is actually a circle, while an ellipse whose eccentricity is 1 is a line segment.)	Pattern_Eccentricity_percentile_0.1	Eccentricity of the most circular structures (lowest 10% eccentricity) on the surface
Area	The actual number of pixels in the region	Pattern_area_mean	Mean area of pillars on the surfaces
Compactness	The mean squared distance of the object's pixels from the centroid divided by the area. A filled circle will have a compactness of 1, with irregular objects or objects with holes having a value greater than 1.	Pattern_Compactness_percentile_0.1 Pattern_Compactness_max	Lowest 10% measured compactness Maximum measured compactness
Radius	The length (in pixels) of the minor axis of the ellipse that has the same normalized second central moments as the region	Pattern_MaximumRadius_mean Pattern_MaximumRadius_max	Mean of the maximum radii on the surface Maximum radii on the surface
Orientation	The angle (in degrees ranging from -90 to 90 degrees) between the x-axis (of the Topo unit) imaged and the major axis of the ellipse that has the same second-moments as the region.	Pattern_Orientation_percentile_0.1	Lowest 10% measured relative orientation of features
Inscribed Circle Radius	A number of circles that can be fitted in gap between pillars. The algorithm is looped until a circle diameter smaller than 6 µm is found.	Inscr_Circl_Radius_0.75_percentile	The radius of the top 25% of inscribed circles

References

[1] Carpenter A. E., Jones T. R., Lamprecht M. R., Clarke C., Kang I. H., Friman O., Guertin D. A., Chang J. H., Lindquist R. A., Moffat J., Golland P., Sabatini D. M. CellProfiler: Image Analysis Software for Identifying and Quantifying Cell Phenotypes. *Genome Biology*, 7 (2006) R100.